nature communications

Article

https://doi.org/10.1038/s41467-025-65308-8

Deleterious variants in the autophagy-related gene *RB1CC1*/FIP200 impair immunity to SARS-CoV-2

Received: 8 July 2025

Accepted: 13 October 2025

Published online: 27 November 2025

Check for updates

Lili Hu[1,2], Renee M. van der Sluis[1,2,152], Kennith Brian Castelino[1,152], Bao-Cun Zhang[1,2], Andreas Ronit[3], Thomas Zillinger[1,2], Marvin Werner[1,2], Sofie Eg Jørgensen[1,2], Anne Louise Hansen[1], Alice Pedersen[1], Ryo Narita[1,2], Line S. Reinert[1,2], Bettina Bundgaard[1,2], COVID Human Genetic Effort*, Christian K. Holm[1], Aurelie Cobat[4,5,6], Jean-Laurent Casanova[4,5,6,7,8], Fulvio Reggiori[1,152], Muriel Mari[1,152], Søren R. Paludan[1,2] & Trine H. Mogensen[1,2,9]

The clinical outcome of SARS-CoV-2 infection spans from asymptomatic viral elimination to lethal COVID-19 pneumonia, which is due to type I interferon (IFN) deficiency in at least 15–20% of cases. We report two unrelated male patients with critical COVID-19 who are heterozygous for rare deleterious variants in *RB1CC1*, encoding the autophagy-related FIP200 protein. Airway epithelial cells genetically deprived of FIP200 or cell lines expressing the *RB1CC1*/FIP200 patient variants exhibit elevated SARS-CoV-2 replication and impaired autophagic flux. The antiviral function of FIP200 is independent of canonical autophagy and type I IFN, but involves the selective autophagy receptor NDP52. We identify a non-canonical function of FIP200 in a novel lysosomal degradation pathway, in which SARS-CoV-2 virions are targeted to single-membrane compartments for degradation of viral RNA in LC3B-positive acidified vesicles. This pathway is impaired in FIP200-deficient cells and in cells expressing FIP200 patient haplotypes. Collectively, we describe a cell-autonomous anti-SARS-CoV-2 restriction pathway, dependent on FIP200 and NDP52, and independent of canonical autophagy and type I IFN, which can underlie critical COVID-19 pneumonia.

Infection by severe acute respiratory syndrome coronavirus 2 (SARS-CoV)-2 can manifest as severe infection with pneumonia, cytokine storm, and systemic disease, causing coronavirus disease 2019 (COVID-19)[1–4]. SARS-CoV-2 is a positive-sense single-stranded (ss)RNA enveloped virus belonging to the beta-coronavirus family. SARS-CoV-2 infects cells through binding of the viral S protein to the cellular ACE2 surface receptor[5,6]. Some studies have suggested varying degrees of infection of non-ACE2-expressing cell types, such as macrophages,

[1]Department of Biomedicine, Aarhus University, Aarhus, Denmark. [2]Center for Immunology of Viral Infections, Aarhus University, Aarhus, Denmark. [3]Department of Infectious Diseases, Copenhagen University Hospital – Amager and Hvidovre Hospital, Hvidovre, Denmark. [4]Laboratory of Human Genetics of Infectious Diseases, Necker Branch, Institut National de la Santé et de la Recherche Médicale (INSERM) U1163, Necker Hospital for Sick Children, Paris, France. [5]Imagine Institute, Paris Cité University, Paris, France. [6]St. Giles Laboratory of Human Genetics of Infectious Diseases, Rockefeller Branch, The Rockefeller University, New York, NY, USA. [7]Howard Hughes Medical Institute, New York, NY, USA. [8]Department of Pediatrics, Necker Hospital for Sick Children, Paris, France. [9]Department of Infectious Diseases, Aarhus University Hospital, Aarhus, Denmark. [152]These authors contributed equally: Renee M. van der Sluis, Kennith Brian Castelino, Fulvio Reggiori, Muriel Mari.*A list of authors and their affiliations appears at the end of the paper.
e-mail: Trine.mogensen@biomed.au.dk

through an ACE2-independent endocytic mechanism representing a largely abortive infection[7]. Cells of the innate immune system sense SARS-CoV-2 infection and trigger the production of type I interferon (IFN), which mediates antiviral activity through autocrine and paracrine IFN receptor (IFNAR)1/2 signaling and induction of IFN-stimulated genes (ISGs)[8]. Accumulating evidence suggests that respiratory epithelial cells and plasmacytoid dendritic cells mainly sense viral double-stranded (ds)RNA and ssRNA through Toll-like receptor (TLR)3 and TLR7, respectively[9–11], whereas cytosolic sensing of SARS-CoV-2 dsRNA intermediates involves retinoic acid-inducible gene (RIG)-I-like receptors[8,12,13]. Importantly, SARS-CoV-2 has evolved a range of mechanisms to evade antiviral responses by targeting specific components of these pathways[14] thereby reducing classical type I IFN production by infected host cells. This raises the possibility that other, alternative antiviral pathways may be important for control of the infection.

The clinical spectrum of human infection with SARS-CoV-2 spans from asymptomatic to severe and lethal COVID-19, but the underlying causes of critical disease pathologies and the extensive interindividual variability in disease severity are still not fully understood. The principal epidemiological risk factor is age, with a risk of death doubling every 5 years from childhood onwards[4,15]. In rare cases, otherwise healthy individuals without the well-established risk factors might experience a severe, fulminant disease course. In some of these patients, critical disease has been ascribed to the presence of inborn errors of TLR3- or TLR7-dependent type I IFN immunity, including defects in TLR3, TLR7, IRF3, IRF7, TRAF3, TBK1, UNC93, IFNAR1/2, TYK2, and STAT2, together accounting for a substantial amount of cases of critical COVID-19 pneumonia[16,17]. Moreover, an even larger proportion of critical COVID-19 cases and deaths has been connected to phenocopies of these inborn errors of immunity (IEI), i.e., the presence of neutralizing auto-antibodies against IFNα, -β, or -ω, thereby effectively interfering with the generated antiviral response[17–19]. These studies demonstrate the essential antiviral role of type I IFN against SARS-CoV-2 and illustrate that specific defects in innate antiviral immunity can underlie critical COVID-19 in individual patients.

In recent years, macroautophagy (hereafter referred to as autophagy) has emerged as an important component in innate and adaptive antiviral immunity, playing non-redundant functions independently of type I IFNs[20–24]. Autophagy is an evolutionary conserved degradation process in all eukaryotic cells, involved in the removal of dysfunctional or unwanted proteins, damaged or excess organelles, and clearance of intracellular pathogens in order to maintain cellular homeostasis[25]. In most cells, autophagy operates at basal levels but can be upregulated by cellular stress, such as nutrient starvation, inflammation, infection, and oxidative stress[25]. These pathogenic or metabolic cues can induce autophagy pathways or other lysosomal degradative pathways. Canonical autophagy is characterized by sequestration of the cargo material to be eliminated by double-membrane vesicles termed autophagosomes[25,26]. The targeting of cargo for autophagy can be mediated by selective autophagy receptors (SARs), which are central for exclusive degradation of specific substrates, including mitochondria, endoplasmic reticulum membranes, and pathogens[27]. A central step in autophagosome biogenesis is the formation of the precursor cisterna known as the phagophore, which involves autophagy-related gene (ATG)9A-positive vesicles, the autophagy-specific class III phosphatidylinositol 3-kinase (PtdIns3K) complex, and the ULK kinase complex, which encompasses ULK1/ ULK2, ATG13, FIP200, and ATG101[26]. This is followed by phagophore elongation and closure, which also entails the recruitment of LC3 family proteins to the phagophore via conjugation to phosphatidylethanolamine (PE), a process referred to as LC3B-I to LC3B-II conversion[26]. Finally, autophagosomes fuse directly with lysosomes, or first with endosomes to form amphisomes, and subsequently with lysosomes to eventually form autolysosomes containing the cargo designated for degradation. Non-canonical forms of autophagy refer to a diverse collection of autophagy-related processes that utilize portions of the autophagy machinery, including LC3 lipidation, for lysosomal degradation of cytosolic content[28], but are distinguished from canonical autophagy by the independence from key autophagy-related proteins or lack of double-membrane structures. Additionally, there is accumulating evidence of non-canonical functions of ATG proteins, where they play a crucial role in pathways other than autophagy, such as in LC3-associated phagocytosis[29–33]. While canonical autophagy seems to have evolved as a homeostatic response to cellular stress and nutrient deprivation, non-canonical autophagic pathways converged on a major aim in containment and suppression of inflammation.

Autophagy pathways cross-talk with and regulate innate immunity in both positive and negative ways through interaction with PRR signaling molecules, such as cGAS, STING, RIG-I, MAVS, IKKβ, IRF3, and many others[34]. In particular, TBK1 plays a central role at the intersection of type I IFN responses and autophagy, since it acts in autophagy initiation, cargo capture, and preparation of autophagosomes for maturation, as well as in type I IFN induction[34]. Autophagy also exerts essential functions in adaptive immunity, where it plays a key role in antigen presentation, including delivery of endogenous antigens for MHC II presentation, elimination of autoreactive T cells in the thymus, and antigen cross-presentation during infection[34]. In the context of viral infections, autophagy may facilitate either proviral or antiviral activities. In regards to the proviral activity, autophagy-related activities can be hijacked to provide membranes for replication or to degrade immune regulators. The antiviral actions of autophagy, in contrast, can drive the turnover of viral components, promote antigen presentation, or enhance cell survival[35]. It has been demonstrated that several coronaviruses induce autophagic processes, although some of these viruses also interfere with the progression of the pathway prior to autophagic degradation[26,36]. Importantly, some aspects of the antiviral functions of ATG proteins may not be attributable to canonical autophagy, but rather represent unconventional functions of these proteins[37–40].

The evidence of antiviral activities of autophagy and ATG proteins emerging from studies in cell systems and mouse models has now started to be supported by human data, through the identification of IEI affecting ATG proteins in patients with infectious diseases. This further provides proof-of-principle of an important immune function of autophagy processes and ATG proteins in human immunology[41]. We previously reported on the identification of defective autophagy in patients with recurrent herpes simplex virus type 2 lymphocytic (Mollaret) meningitis carrying variants in *ATG4A* and *LC3B2* genes[42], and in another study, we described an *ATG7* variant with impaired antiviral function in a poliomyelitis patient[43]. Recently, impaired cGAS-induced autophagy was implicated in the pathogenesis of herpes simplex encephalitis in a patient with a dominant negative TBK1 mutation[44]. To explore and discover novel antiviral functions of autophagy and ATG proteins in human immunology and disease pathogenesis, we tested the hypothesis that IEI in genes involved in autophagy-related pathways may impair antiviral immunity to SARS-CoV-2 and underlie critical COVID-19.

Results

Identification of rare missense variants in *RB1CC1*/FIP200 in two unrelated patients with critical COVID-19

Within a cohort of 56 patients with critical COVID-19, we performed whole-exome sequencing (WES) to search for rare genetic variants under a hypothesis of autosomal dominant or recessive inheritance, or X-linked recessive inheritance. Variants were filtered based on deleteriousness and rarity. Only rare non-synonymous and essential splicing variants in genes with a gene damage index (GDI) below 13.83, minor allele frequency (MAF) < 0.001 in the Genome Aggregation Database (gnomAD), and a combined annotation-dependent depletion (CADD) score higher than the mutation significance cut-off (MSC) and

>20 were kept. (See Methods for details and Supplementary Table 1 for gene variants). In this process, the exome was also examined for deleterious variants in any of the genes known to be related to IEI according to the most recent guidelines[45], as well as for variants in any of the genes previously described to be disease-causing or associated to critical COVID-19[46], none of which were identified. This genetic analysis led to the identification of two different monoallelic missense variants in the *focal adhesion kinase family interacting protein of 200 kD* (*FIP200*)/*RB1-inducible coiled-coil protein 1* (*RB1CC1*) gene in two patients. According to the Human Protein Atlas, FIP200 protein is expressed in all cell types and tissues, but particularly highly abundant in the respiratory tract and the female reproductive tract [https://www.proteinatlas.org/ENSG00000023287-RB1CC1/tissue]. P1 is a previously healthy 56-year-old white male without any comorbidities and with critical COVID-19 pneumonia with bilateral infiltrations on chest X-ray and acute respiratory distress syndrome, who was admitted to the intensive care unit (ICU). P2 is a 31-year-old white male without any comorbidities admitted to hospital with critical COVID-19 pneumonia, marked pulmonary infiltrations requiring 12 L oxygen supplementation, and treated with remdesivir and dexamethasone in the ICU (Fig. 1a, b). Both patients were unvaccinated and tested positive for the SARS-CoV-2 Wuhan B1 strain (See Supplementary for inclusion criteria and detailed clinical history and laboratory values). The identified variants in *FIP200* c.164C>T; p.Ala55Val in patient (P)1 and c.1420C>T; p.Arg474Cys in P2, are predicted by Sorting Intolerant From Tolerant (SIFT) software to be damaging (Fig. 1c). The CADD scores are 22 and 32 for A55V (P1) and R474C (P2), respectively, well above the MSC of 3.313 and therefore among the 2% most deleterious variants (Fig. 1c). Two out of 56 represents an enrichment, when compared with the general population. Sanger sequencing confirmed the variants. The identified variants in patients are localized in the N-terminal part of the FIP200 protein (Fig. 1d). Alignment of the amino acid sequence around the identified variants across species reveals a high degree of evolutionary conservation suggesting functional importance of the mutated residues (Fig. 1e). The parents of P1 have died and we do not have access to material from the parents of P2. The two children of P1 did not experience any severe disease manifestations with SARS-CoV-2 infection (genetic analysis of whom was declined), and P2 does not have children, thereby limiting the possibility to determine inheritance and penetrance of the identified FIP200 variants.

Population genetics of *RB1CC1*/FIP200

The two variants in *RB1CC1*/FIP200 identified in the patients are rare, with frequencies in gnomAD v4.1.0 of 1.9×10^{-4} and 1.6×10^{-5} for p.Ala55Val (P1) and p.Arg474Cys (P2), respectively (Fig. 1c, f). Only two homozygotes have been reported for A55V in gnomAD v4.1.0 in two individuals of African/African American ancestry, among whom the frequency is the highest (3.5×10^{-3}). No homozygotes have been reported for the variant of P2 (R474C), and the maximum allele frequency observed is 8.8×10^{-5} in individuals of South Asian ancestry. The *RB1CC1*/FIP200 gene is highly conserved and under strong negative selection, as demonstrated by its low loss-of-function observed/expected upper bound fraction (LOEUF) score of 0.29, indicating strong depletion of predicted loss-of-function variants in the general population, and a markedly negative CoNeS score of −1.7, reflecting strong selective pressure (Fig. 1g). Altogether, these metrics are consistent with autosomal dominant inheritance[47,48]. For missense variants in *RB1CC1/FIP200* with CADD > 20 and MAF < 0.001, comparing two patients in the cohort of 56 patients against 8885 individuals among a total of 807,162 individuals listed in gnomAD yields an odds ratio of 3.328 (95 % CI [0.8112–13.65], p = 0.1267 Fisher's exact test), suggesting accumulation of *RB1CC1/FIP200* missense variants in the patient cohort although not significant, possibly because some of the *RB1CC1/FIP200* missense variants present in gnomAD are not deleterious. The cumulative frequency (cMAF) in gnomAD v4.1.0 of all reported pLoF (including stop codon variants) for *RB1CC1/FIP200* is 2.5×10^{-4} with no homozygous reported. The cMAF of rare ($<10^{-3}$) missense or inframe indels with CADD > 20 in gnomAD v4.1.0 is 5.8×10^{-3} with 24 homozygous reported. Focusing on the N-terminal domain of FIP200, we found a 6.6-fold enrichment of rare ($<10^{-3}$) missense or pLoF variants with CADD > 20 in patients (cMAF = 2/112 = 0.018) versus gnomAD v4 (cMAF = 0.0024). Given the cMAF in gnomAD, we estimated that the probability of observing at least two carriers of such variants in the N-terminal domain among 56 patients was 0.03.

Reduced expression and function of FIP200 in the patient cells

Analysis of FIP200 expression in patients PBMCs showed unaltered FIP200 levels in P1, whereas FIP200 levels were markedly reduced in P2 (Fig. 1h). To examine whether autophagy responses were disturbed in the patients, monocyte-derived macrophages (MdMs) were generated from PBMCs. MdMs have been demonstrated to mount an inflammatory response to SARS-CoV-2 infection, although the virus does not establish productive infection in these cells[49–52]. We observed reduced LC3B-I to LC3B-II conversion at steady state in patient MdMs compared to control, both in untreated cells and in the presence of rapamycin, EBSS (a starvation medium to stimulate autophagy), or SARS-CoV-2 (Fig. 1i, j), suggesting impaired basal and inducible autophagy in cells from patients carrying the identified FIP200 variants.

Viral requirements for induction of autophagy by SARS-CoV-2 in a range of infection models

To evaluate autophagy in hACE2-expressing human pulmonary A549 (A549-hACE2) cells, we first induced canonical autophagy using EBSS starvation or rapamycin treatment to inhibit the mTOR pathway. Autophagy induction was assessed by monitoring the autophagy markers LC3B-I, LC3B-II, and p62. (Supplementary Fig. 1a–c). To investigate the effect of SARS-CoV-2 on autophagy, pulmonary epithelial-like A549-hACE2 cells were infected with SARS-CoV-2 (B.1). We observed dose-dependent enhancement of LC3B-I to LC3B-II conversion, but no significant decrease in p62 levels (Supplementary Fig. 1d–f). Notably, the LC3B-II:LC3B-I ratio and p62 levels were increased upon treatment with the lysosomal inhibitor bafilomycin A1 (BafA1), thus demonstrating activation of autophagic flux[53] (Supplementary Fig. 1d–f). Moreover, immunofluorescence (IF) staining for LC3B and LAMP1 revealed accumulation of LC3B-positive puncta and lysosome compartments in the infected cells at 24 h post-infection (pi) (Supplementary Fig. 1g–j). The finding of SARS-CoV-2-induced autophagy in A549-hACE2 cells was confirmed in VERO E6 cells as well as in physiologically relevant primary human and murine model systems, namely the air–liquid interface (ALI) respiratory epithelial cell model and transgenic K18-hACE C57BL/6J mice, respectively (Supplementary Fig. 1k–r). These data demonstrate that autophagy is induced upon SARS-CoV-2 infection in cells and tissues relevant for COVID-19 pathogenesis. When comparing autophagy induction by different SARS-CoV-2 variants, we found differential potency in inducing autophagy, with the SARS-CoV-2 Delta variant (subtype B.1.617.2) exhibiting the strongest autophagy-inducing activity (Supplementary Fig. 2a–d). To uncover early events in SARS-CoV-2 replication that trigger autophagy, we first correlated the temporal development of replication and autophagy activation and noted that the accumulation of SARS-CoV-2 RNA and nucleocapsid (NC) protein at 2 h and 6 hpi, respectively, correlated with elevation of LC3B-II:LC3B-I ratios at 6 hpi (Supplementary Fig. 2e–h). The notion that viral replication triggers autophagy was further supported by observing that this process was blocked by the viral polymerase inhibitor Remdesivir, and to a lesser extent by the viral protease inhibitors Lopinarvir/Ritonavir in a dose-dependent manner (Supplementary Fig. 2i, j). Finally, UV inactivation of SARS-CoV-2 prior to addition to cell cultures completely abolished induction of autophagy (Supplementary Fig. 2k–m). Collectively, SARS-CoV-2 activates autophagy in multiple physiologically relevant

https://doi.org/10.1038/s41467-025-65308-8

a

Clinical information	P1	P2
Age	56	31
Gender	Male	Male
N days of hospitalization/ICU	14	15

b

c

Genetic information	P1	P2
Gene symbol	*RB1CC1/ FIP200*	*RB1CC1/ FIP200*
Gene name	RB1 Inducible Coiled-Coil 1	RB1 Inducible Coiled-Coil 1
Transcript ID	NM_014781.5	NM_014781.5
Transcript variant	c.164C>T	c.1420C>T
Protein variant	p.A55V	p.R474C
Translation impact	Missense	Missense
CADD	22	32
MSC	3.313	3.313
GDI Phred	3.307	3.307
SIFT function prediction	Damaging	Damaging
GnomAD frequency	1.9×10^{-4}	1.6×10^{-5}
Inheritance	Heterozygous	Heterozygous

d

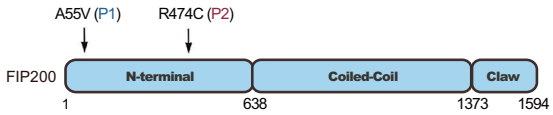

e

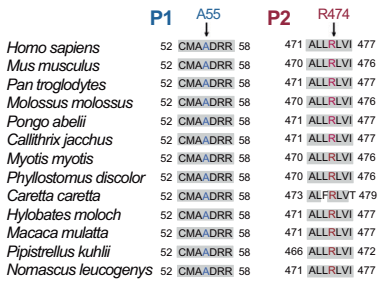

f

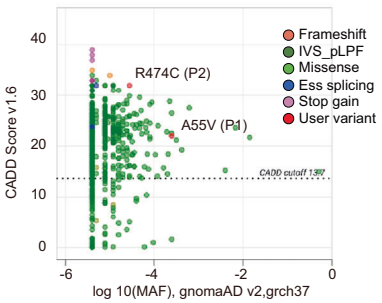

g

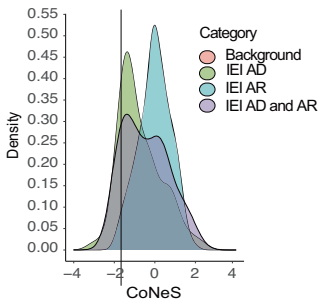

h

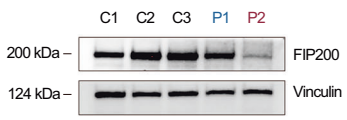

i

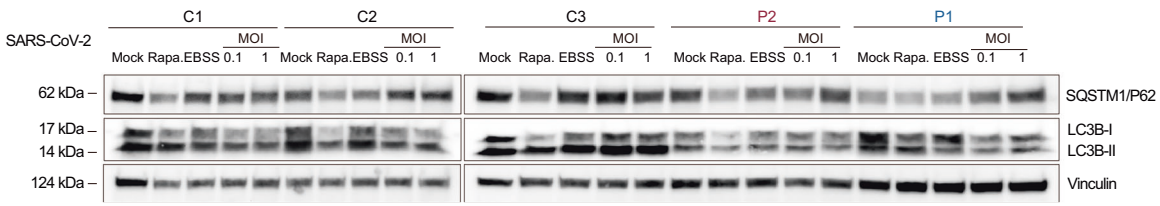

j

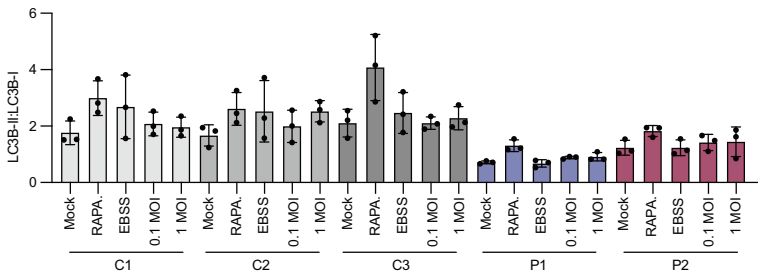

cellular and model systems in a manner dependent on active viral replication.

Increased susceptibility to SARS-CoV-2 infection in FIP200-deficient cells

In order to evaluate the role of FIP200 on antiviral immunity, polyclonal and monoclonal A549-hACE2 cells lacking FIP200 were generated. Strikingly, FIP200 deficiency in polyclonal cultures was associated with strongly enhanced SARS-CoV-2 replication, measured by viral RNA levels by RT-qPCR (Fig. 2a), NC protein levels by immunoblotting (Fig. 2b), and viral titers by using the TCID50 assay (Fig. 2c; Supplementary Fig. 3a, b). This was accompanied by accumulation of p62 in FIP200-deficient cells, a phenotype consistently observed in the absence of FIP200 (Supplementary Fig. 3c). This was

Fig. 1 | Identification of potentially disease-causing rare variants in the autophagy-related gene FIP200 in patients with critical COVID-19. a Clinical information about patients P1 and P2. **b** Chest X-ray of P1 at day 2 of hospitalization. **c** Summary of genetic information and predictions for the *FIP200* variants identified in P1 (c.164C>T; p.Ala55Val) and P2 (c.1420C>T; p.Arg474Cys). **d** Schematic overview of FIP200 structure, which includes an N-terminal domain, a coiled-coil domain, and a C-terminal claw domain. The identified variants are marked. **e** Alignment of the amino acid sequence around the identified mutations in P1 (left) and P2 (right) across species. **f** Minor allele frequency (MAF) and combined annotation-dependent depletion (CADD) scores of the variants reported in gnomAD for P1 and P2. The dotted line corresponds to the mutation significance cut-off (MSC). **g** Analysis of the CoNeS Impact on density of FIP200. AD autosomal dominant, AR autosomal recessive. **h** FIP200 protein levels of FIP200 evaluated by immunoblotting of whole cell lysates from P1, P2, and 3 healthy controls (C1–C3) monocyte-derived macrophages (MdMs). The experiments were repeated three times independently with similar results. **i** MdMs from P1, P2, and 3 controls (C1–C3) were subjected to Earle's Balanced Salts (EBSS) starvation for 2 h, treated with 500 nM rapamycin for 24 h, or infected with SARS-CoV-2 (B.1) at different MOIs for 24 h, then analyzed by immunoblotting. **j** The LC3B-II to LC3B-I ratio in the experiment presented in (**i**) was quantified by densitometry. (n = 3). Data are presented as mean ± SD from three independent experiments. Source data are provided as a Source data file.

also observed in clonal FIP200-deficient cultures (Fig. 2d, Supplementary Fig. 3d–g). To investigate whether this antiviral effect occurs early during infection, we measured SARS-CoV-2 RNA levels at 2, 6, and 16 h post-infection. Enhanced viral replication was already apparent in FIP200-deficient cells compared to controls at 6 and 16 h, but not at 2 hpi (Supplementary Fig. 3g–j). To further examine the antiviral effect of FIP200, we overexpressed FIP200 to investigate if the protein was sufficient to reduce SARS-CoV-2 replication. Indeed, overexpression of FIP200 in A549-hACE2 cells resulted in significant reduction of SARS-CoV-2 RNA levels, close to levels achieved with the ISG-inducing transcription factor IRF1 (Fig. 2e)[54]. Importantly, reconstitution of FIP200 expression in FIP200 KO cells resulted in significantly reduced SARS-CoV-2 replication (Fig. 2f). Examination of cells by IF revealed pronounced accumulation of viral Spike protein in clones lacking FIP200 (Fig. 2g, h and Supplementary Fig. 3k, l). Finally, to test the physiological relevance of FIP200 deficiency in control of SARS-CoV-2 in the human airways, we infected ALI cultures engineered to be deficient in FIP200 and found significantly enhanced SARS-CoV-2 replication (Fig. 2i–k). Altogether, these results demonstrate that FIP200 is essential for control of SARS-CoV-2 infection in airway epithelial cells and support the hypothesis that individuals carrying functionally deleterious variants are susceptible to develop severe COVID-19.

Pulmonary A549-hACE2 cells expressing patient FIP200 variants exhibit increased SARS-CoV-2 replication

To functionally investigate the FIP200 variants identified in the patients, we generated base-edited CRISPR homology-directed repair (HDR) monoclonal cell lines from the hypotriploid A549-hACE2 cells. The cell lines carried the patient missense mutations as knock-in (KI), i.e., A55V for P1 (FIP200 KI P1) and R474C for P2 (FIP200 KI P2) (Supplementary Fig. 4a, b). After infection with SARS-CoV-2, we observed significantly increased SARS-CoV-2 replication at RNA level and virus yield assay in cells expressing the patient variants and FIP200-deficient cells in comparison to the WT controls (Fig. 3a, b). For comparison we also generated A549-hACE2 cell lines expressing the two most frequent (MAF > 10^{-3}) FIP200 variants in the general population as reported in gnomAD: FIP200 D211N (Frequency > 10^{-3}; CADD score > 20) and FIP200 T234M (most frequent variant; CADD score 9) (Supplementary Fig. 4c). These haplotypes both showed SARS-CoV-2 replication levels comparable to control cells, without exhibiting any significant loss of antiviral effect, suggesting that deleterious FIP200 variants are very rare in the general population (Supplementary Fig. 5a). Next, we employed RNA scope technology to specifically detect SARS-CoV-2 genomic (+sense) and transcribed (−sense) RNA by IF in cell lines depleted for FIP200 or expressing the P2 FIP200 variant (hereafter used to model the patient variant). The results showed that FIP200 KO cells exhibited a marked increase in both genomic and transcribed viral RNA. Likewise, cells harboring the FIP200 KI P2 variant displayed significantly higher levels of genomic viral RNA and an increase in transcribed viral RNA (Fig. 3c–e and Supplementary Fig. 5b).

Cells expressing patient FIP200 variants exhibit enhanced ultrastructural signs of infection

To explore the effects of FIP200 deficiency on SARS-CoV-2 replication events at the ultrastructural level, WT, FIP200 KO, and FIP200 KI P2 A549-hACE2 cells were examined by transmission electron microscopy (TEM) (Fig. 3f–i). The ultrastructural analysis of the non-infected cells did not reveal evident morphological differences between these cell lines (Supplementary Fig. 5c). Upon infection with SARS-CoV-2, the three examined cell lines showed the intracellular structures that characterize the replication cycle of coronaviruses, including the double-membrane vesicles (DMVs), which are considered as the major replication sites, the ER-associated spherules, which represent the main site of virion assembly, and the large virion-containing vacuoles (LVCVs), which are Golgi-derived compartments that have expanded to accommodate the enhanced secretion of virions[55] (Fig. 3f). Importantly the number of cells showing signs of infection was significantly higher in the FIP200 KO cells in comparison to the WT, with the FIP200 KI P2 cells having an intermediate phenotype (Fig. 3f, g), with the average diameters of structures associated with SARS-CoV-2 replication—such as spherules and DMVs—were comparable among these cells (Supplementary Fig. 5d, e). Quantification of LVCVs per cell section showed a more pronounced formation of virions in the absence of FIP200 (Fig. 3f, h), with a similar average diameter of virions within LVCVs (Supplementary Fig. 5f, g). Consistent with this, we also detected higher levels of electron-dense vacuole-containing virions appearing as dark vacuoles (DVs) per cell section in both FIP200 KO and FIP200 KI P2 cells compared to WT cells (Fig. 3f, i). However, there was no significant difference in the average number of virions per DVs, although the average diameter of virions in DVs under the WT condition appeared smaller (Supplementary Fig. 5h, i). In the presence of BafA1, the ultrastructures from the infected cells again revealed marked differences between FIP200 defective cell lines compared to WT, including significantly enhanced signs of infection (Supplementary Fig. 5j, k), increased number of LVCVs (Supplementary Fig. 5j, l), and dark vacuole virion clusters (Supplementary Fig. 5j, m).

Preserved LC3B-I to LC3B-II conversion in response to SARS-CoV-2 in FIP200-deficient cells

The results presented above suggest defects in FIP200 to be associated with increased susceptibility of airway epithelial cells for SARS-CoV-2 infection. We next examined constitutive and induced autophagy in A549-hACE2 WT and FIP200-deficient cells. As expected, FIP200-deficient cells showed decreased basal autophagy and failed to induce autophagic flux upon treatment with rapamycin or EBSS (Supplementary Fig. 6a–f). The reduced autophagy flux was also evidenced by the accumulation of p62 (Supplementary Fig. 6a–f). Interestingly, when examining virus-induced autophagy, the infection-induced increase in LC3B-II:LC3B-I observed in both parental A549-hACE2 and AAVS1 KO cells was not altered in FIP200-deficient cells (Fig. 4a, b). This was corroborated by IF analysis of p62, which revealed increased numbers and areas of p62 puncta in both WT and FIP200 KO cells following SARS-CoV-2 infection (Supplementary Fig. 6g–i). To understand the preserved LC3B-I to

https://doi.org/10.1038/s41467-025-65308-8

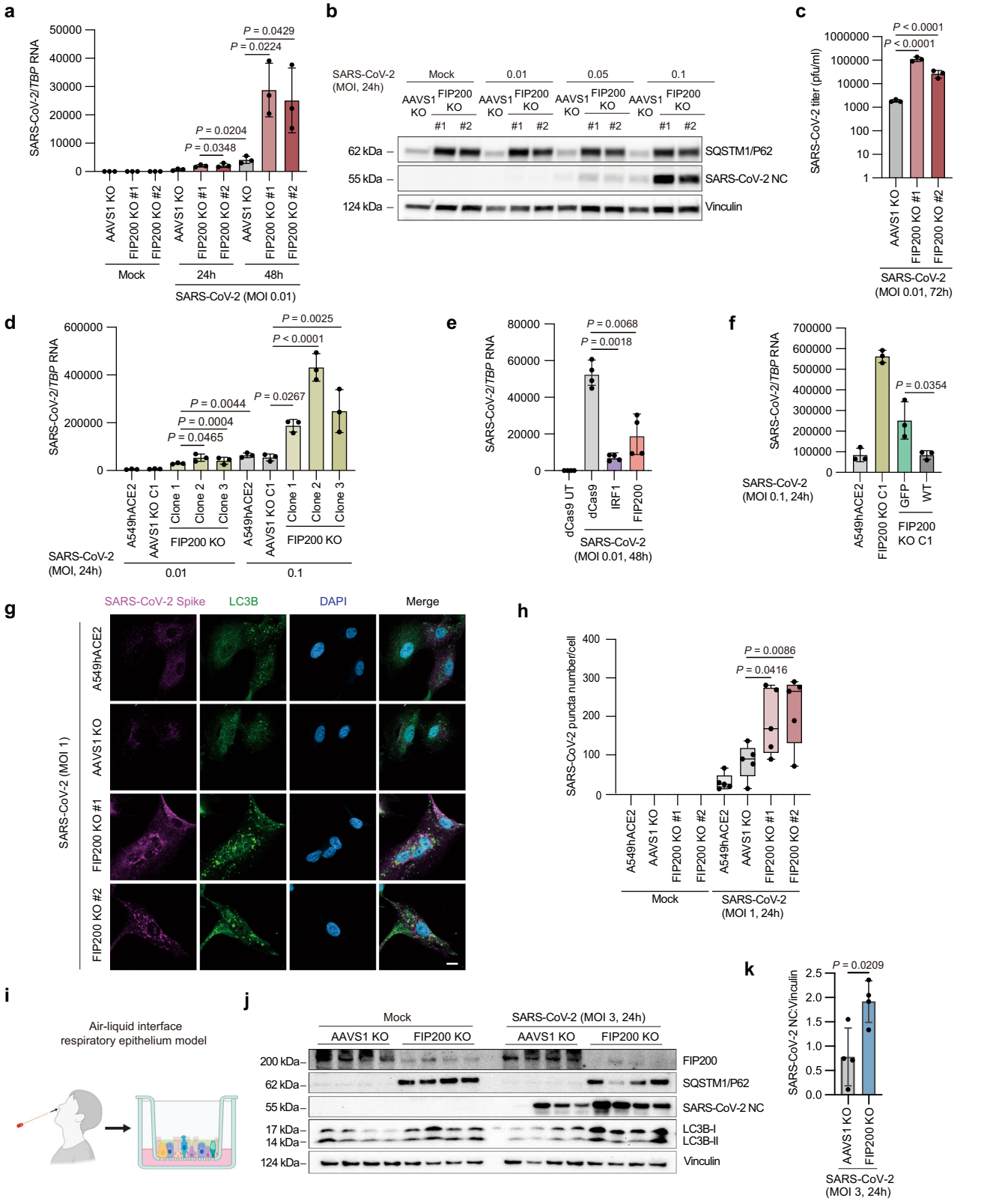

LC3B-II conversion in FIP200-deficient cells in response to SARS-CoV-2, in contrast to the defective induction of autophagy by Rapamycin and EBSS, we investigated other possibilities for LC3B conversion in other cellular processes, which are collectively referred to as ATG8ylation[56]. One such mechanism is lipophagy, whereby virus-induced accumulation of lipid droplets can promote LC3B-I to LC3B-II conversion in a FIP200-independent manner[57]. Indeed, we found that in response to SARS-CoV-2 infection, the number of cytoplasmic lipid droplets, LC3B-positive punctae, and colocalization of the two increased in both A549-hACE2 WT and A549-hACE2 FIP200-deficient cells (Supplementary Fig. 7a–d), thereby providing a plausible but not exclusive explanation for the partly retained total LC3B-I to LC3B-II conversion in FIP200 KO cells in response to SARS-CoV-2 infection.

Fig. 2 | Increased SARS-CoV-2 replication in FIP200-deficient cells. **a**–**c** Polyclonal AAVS1 KO and FIP200 KO (guide #1/#2) A549-hACE2 cells were infected with SARS-CoV-2 at the indicated MOIs and time points. **a** RNA extracted at 24/48 h p.i. for RT-qPCR. Data normalized to TBP (n = 3). **b** Cell lysates at 24 h p.i. analyzed by immunoblotting. **c** Supernatants at 72 h p.i. were titrated by TCID50 (n = 3). **d** WT, monoclonal AAVS1 KO and FIP200 KO (clones 1–3) A549-hACE2 cells were infected at indicated MOIs (24 h), RNA extracted for RT-qPCR. Data normalized to TBP (n = 3). **e** CRISPRa of FIP200 or IRF1 overexpressing cells were infected at MOI 0.01 for 48 h, RNA extracted for RT-qPCR. Data normalized to TBP (n = 4). **f** Monoclonal FIP200 KO (clone 1) cells were transduced with lentivirus expressing FIP200 or GFP. Cells infected at MOI 0.1 for 24 h, RNA extracted for RT-qPCR. Data normalized to TBP (n = 3). **g** Polyclonal AAVS1 KO and FIP200 KO (guide #1/#2) cells were infected for 24 h and stained for SARS-CoV-2 Spike protein and LC3B. Scale bar, 10 μm. **h** Quantification of SARS-CoV-2 positive punctate structures per cell in the experiment shown in (**g**) was determined by ICY software. (n = 5, each data point represents the mean value per image). Box plots show median (center line), 25th–75th percentiles (box), and min–max values (whiskers). **i** Illustration of the air–liquid interface (ALI) respiratory epithelium model. Created in BioRender. Paludan, S. (2025) https://BioRender.com/g8fje2r. **j** ALI cells were infected at MOI 3. Cell lysates were analyzed by immunoblotting. **k** SARS-CoV-2 NC to vinculin ratio from (**j**) was quantified by densitometry (n = 4). All data are representative of at least three independent experiments. **g** shows representative images. Quantification shown as mean ± SD, statistical analysis was carried out using one-way ANOVA with two-sided Dunnett's multiple comparison correction (**a**, **c**, **d**, **h**), Brown-Forsythe Welch ANOVA tests with two-sided Dunnett's T3 multiple comparison correction (**e**), and two-sided Student's t test (**f**, **k**). Source data are provided as a Source data file.

Impaired autophagy flux in cells with FIP200 deficiency

Given that LC3B-I to LC3B-II conversion alone does not reflect a measure of functional autophagy[56,58], we next verified the autophagic flux by treating cells with BafA1 inhibiting lysosomal acidification. As expected, treatment of SARS-CoV-2-infected control A549-hACE2 and AAVS1 cells with BafA1 led to further accumulation of LC3B-II and an elevated LC3B-II:LC3B-I ratio compared to the situation without BafA1, indicating intact autophagic flux (Fig. 4a, b). In contrast, addition of BafA1 to SARS-CoV-2-infected FIP200-deficient A549-hACE2 cells did not increase the LC3B-II:LC3B-I ratio compared to cells not treated with BafA1, reflecting a significantly reduced autophagy flux in these cells (Fig. 4a, b). Similar results were observed in the polyclonal FIP200 KO cells following SARS-CoV-2 infection (Supplementary Fig. 7e–g). These results were confirmed by IF staining, where we observed augmentation in the number of LC3B-positive puncta upon BafA1 in SARS-CoV-2-infected AAVS1 control but not FIP200 KO cells (Fig. 4c, d). Likewise, we observed reduced virus-induced autophagy flux compared to controls in KI cell two clones expressing the FIP200 variants from P1 (FIP200 KI P1) or P2 (FIP200 KI P2) mimicking patient cells (Fig. 4e, f, Supplementary Fig. 7h), collectively demonstrating impaired autophagy flux in FIP200 deficiency.

Absence of virions in autophagosomes

To further explore the autophagy machinery at the ultrastructural level, we used the above mentioned TEM preparations to compare A549-hACE2 WT, FIP200 KO and FIP200 KI P2 cells, specifically focusing on autophagosome to inspect their cargoes (Fig. 4g). In agreement with the core function of FIP200 in this pathway, we did not detect double-membrane autophagosomes in FIP200 KO cells, and their abundance was reduced in FIP200 KI P2 cells in comparison to the control (Fig. 4h). It is noteworthy, that the autophagosomes observed in WT and FIP200 KI P2 cells did not contain discernible structures associated with SARS-CoV-2 replication, such as virions, DMVs, spherules, or LVCVs (Fig. 3f, Supplementary Fig. 7i, j). Accordingly, double-membrane autophagosomes do not appear to be directly involved in the degradation of morphologically identifiable viral components or replication structures. In the presence of BafA1, we again observed absence of virus-related structures in the inner vesicles containing undigested autophagosomal content in WT cells. These data re-iterate that the antiviral activity of FIP200 likely does not involve the direct degradation of viral components by autophagy.

The antiviral activity of FIP200 is exerted independently of canonical autophagy and type I IFN responses

To further explore the autophagic requirements of for the identified antiviral activity of FIP200, we examined the effect of deleting ATG5, which is also essential in canonical (macro)autophagy[22]. Interestingly, SARS-CoV-2 replication was similar in ATG5 KO and control AAVS1 KO cells lines (Fig. 5a), despite the loss of ATG5-mediated canonical autophagic flux and a strong reduction in the conversion of LC3B-I into LC3B-II as expected (Fig. 5b, Supplementary Fig. 8a). Given the observation of increased SARS-CoV-2 replication in cells lacking FIP200, we investigated whether the loss of antiviral capacity might be related to defective IFN immunity, since IEI with impaired induction of or responses to IFN have previously been reported in patients with critical COVID-19[16]. Measurement of transcripts for IFNs, ISGs, and other cytokines in WT and FIP200 KO A549-hACE2 cells infected with SARS-CoV-2 demonstrated preserved, and for many genes even enhanced, induction of the antiviral and inflammatory genes (Fig. 5c–e, Supplementary Fig. 8b–d). Particularly, *IFNB1* and *IFNL1* were significantly elevated in FIP200 KO cells upon SARS-CoV-2 infection compared to infected AAVS1 control cells. When extending the same analysis to patient cells, we observed some reduction in production of type I IFNs in PBMCs from P1, but not from P2 (Supplementary Fig. 8e, f). In addition, IFNγ levels were significantly elevated in cells from both patients, while TNFα was elevated only in cells from P1 (Supplementary Fig. 8g, h). It should be noted that the observations from patient cells might be influenced by treatment of the critically ill COVID-19 patients with immunosuppressive glucocorticoids at the time of the sampling. Collectively, since we did not observe major defects in cytokine and type I IFN responses in cells lacking FIP200, nor in patient PBMCs, we infer that the loss of antiviral activity of FIP200 is not directly interconnected with impaired type I IFN or cytokine production.

Elevated viral replication in cells deficient in the selective autophagy receptor NDP52

FIP200 is a key player in selective types of autophagy due to its role in connecting the SARs with the ATG machinery[59,60]. Therefore, we examined whether select SARs, including FAM134B and NDP52, may function together with FIP200 in to exert antiviral activity in SARS-CoV-2-infected cells. First, we examined the effect of the ER-integral membrane protein FAM134B, one of the SARs mediating ER-phagy[61,62], which has been ascribed a proviral role during SARS-CoV-2 infection[63,64]. Depletion of FAM134B resulted in reduced SARS-CoV-2 replication in the context of unaltered autophagy induction measured by LC3B-II:LC3B-I ratio (Supplementary Fig. 9a–d). This is in agreement with previous studies and suggests a proviral role of FAM134B, which is therefore unlikely to be directly involved in the antiviral activity of FIP200 against SARS-CoV-2. NDP52 is a cytosolic ubiquitin-binding SAR known to directly interact with FIP200 and to mediate both virus-induced autophagy and modulation of various aspects of immunity[65,66]. Interestingly, similar to the observation following depletion of FIP200, disruption of the NDP52 gene resulted in elevated SARS-CoV-2 viral load (Fig. 5f, Supplementary Fig. 9e, f), suggesting an antiviral role of this SAR in SARS-CoV-2 infection. We also noted that NDP52 levels decreased upon SARS-CoV-2 infection in WT cells, indicating NDP52 participation in degradative processes. (Supplementary Fig. 9e). We further generated hACE2-A549 cells deficient in both FIP200 and NDP52, and found that SARS-CoV-2 replication was not further elevated in these FIP200-NDP52 double KO cells compared to the FIP200 and NDP52 single KO cells (Fig. 5g–i and Supplementary

https://doi.org/10.1038/s41467-025-65308-8

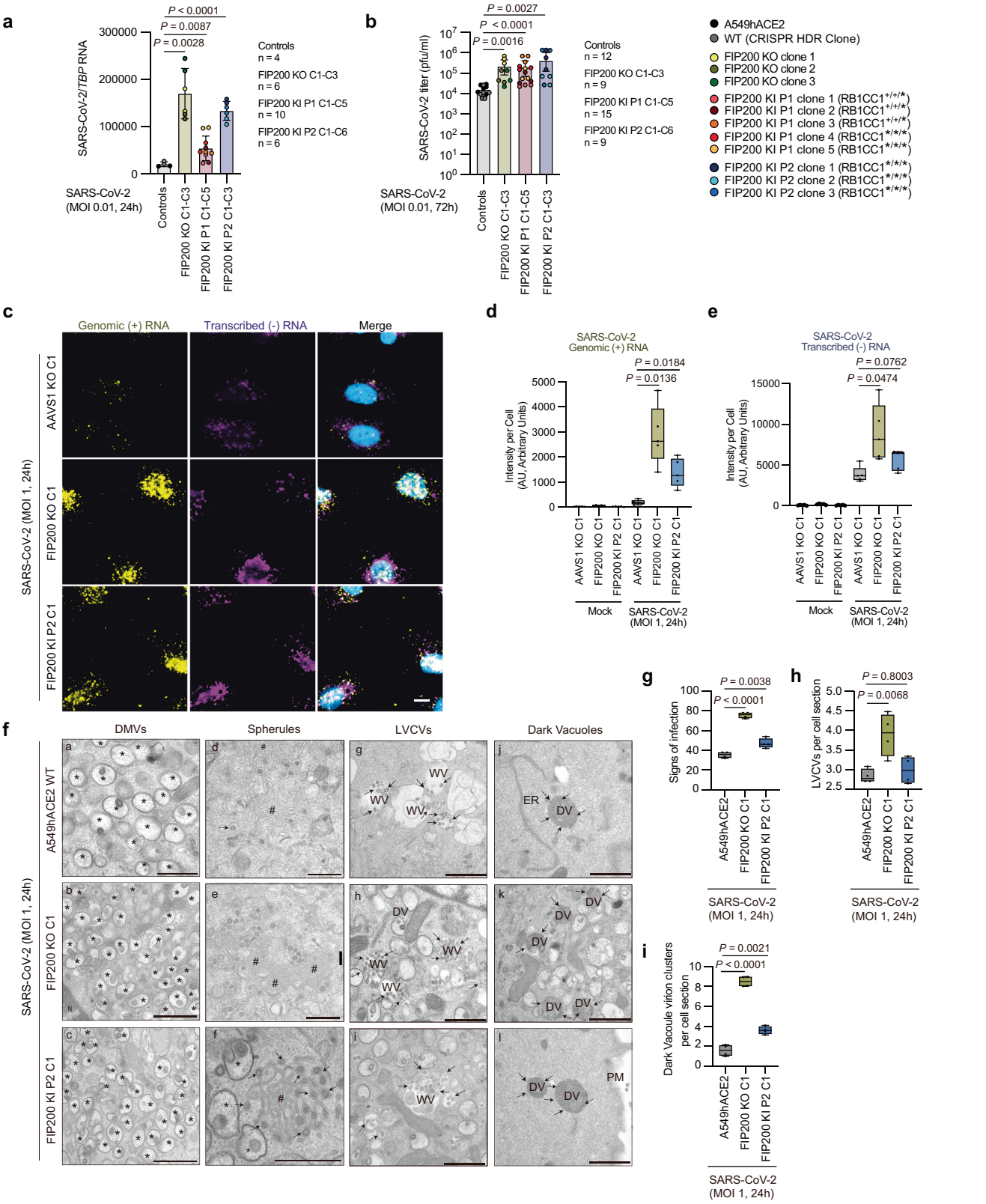

Fig. 9g). These results suggest that NDP52 acts in the same antiviral pathway as FIP200.

FIP200 is essential for degradation of SARS-CoV-2 RNA in acidified LC3-positive vesicles

Finally, we wanted to mechanistically characterize the FIP200-dependent antiviral activity. When following the dynamics of viral RNA in control and FIP200 KO cell lines over time, we observed that the difference between the genotypes was evident at 6 but not 2 h post-infection (Fig. 6a), suggesting that FIP200 does not affect viral cell entry or incoming delivery of viral RNA. To examine whether FIP200 impacts on the stability of viral macromolecules, we infected the cells with SARS-CoV-2 for 24 h and subsequently treated with Remdesivir to block further viral replication. This allowed us to assess

Fig. 3 | Increased SARS-CoV-2 replication in pulmonary A549A-hACE2 cells harboring the FIP200 variants identified in P1 and P2. a, **b** Monoclonal hypotriploid hACE2-A549 cells carrying patients FIP200 variants were infected with SARS-CoV-2 (MOI 0.01). **a** RT-qPCR at 24 h p.i. Data normalized to TBP (mean ± SD). **b** Supernatants at 72 h p.i. were titrated by TCID50. ⁺, WT allele; *, patient variant. (mean ± SD). **c** Monoclonal AAVS1 clone 1, FIP200 KO clones 1, and FIP200 KI P2 clone 1 were infected (MOI 1, 24 h) and processed for RNA Scope. Scale bar, 10 μm. Quantification of intensity of genomic (+) RNA (**d**) or transcribed (−) RNA (**e**) in (**c**) was analyzed by ZEISS ZEN lite software. (mean ± SD, n = 5, each data point represents the mean value per image). **f** WT, monoclonal FIP200 KO clone 1 and FIP200 KI P2 clone 1 A549-hACE2 cells were infected (MOI 1, 24 h) and processed for transmission electron microscopy (TEM). *, DMVs double-membrane vesicle; #, spherules; LVCV large virion-containing vacuole; Arrows, virions in the spherules and LVCVs; WV white vacuole, DV dark vacuole, ER endoplasmic reticulum, PM plasma membrane. Scale Bar, 1 μm. **g** Percentage of cells showing sign of infection as an aggregate score of detection of DMVs, spherules, LVCVs, or virion-containing DV. Quantification of LVCVs (**h**) and virion-containing DV (**i**). Quantifications performed by examining for each condition 200 randomly selected cell profiles from four independent grids (mean ± SEM, n = 4). Data are representative of three independent experiments (**a**–**e**), **c**, **f** show representative images. Statistical analysis was performed using Brown-Forsythe Welch ANOVA tests with two-sided Dunnett's T3 multiple comparison correction (**a**, **b**, **d**, **e**), and one-way ANOVA with two-sided Dunnett's multiple comparison correction (**g**–**i**). Box plots show median (center line), 25th–75th percentiles (box), and min–max values (whiskers) (**d**, **e**, **g**–**i**). Source data are provided as a Source data file.

the decay of viral RNA over time. Interestingly, we observed a progressive decrease in viral RNA in WT cells, which was significantly reduced in FIP200-deficient cells (Fig. 6b). As described above, we did not observe virions in double-membrane autophagosomes (Fig. 4g). Interestingly, however, ultrastructural analysis revealed virions inside single-membrane degradative compartments (DGCs), which entail lysosomes, amphisomes, and autolysosomes (Fig. 6c). Quantification of these structures showed a strong decrease in the percentage of DGCs containing virions in FIP200 KO cells and FIP200 KI P2 in comparison to WT cells (Fig. 6c, d). These data demonstrate that *de-novo*-produced virions and viral macromolecules, including RNA, undergo degradation through a FIP200-dependent lysosomal or late endosomal pathway.

Loss of acidified LC3B-II positive virus-containing vesicles in FIP200-deficient cells

The results above suggest that SARS-CoV-2 infection triggers FIP200-dependent autophagy flux (Fig. 4a) and a pathway mediating degradation of virions, including RNA (Fig. 6b, c). To further test this, we evaluated the induction of acidification of LC3B-positive vesicles and its dependence on FIP200. SARS-CoV-2 infection did indeed induce puncta positive for both LC3B and lysotracker (Fig. 6e–g, Supplementary Fig. 10a). Interestingly, the percentage of acidic LC3B-positive vesicles was significantly lower in infected FIP200-deficient cells compared to WT (Fig. 6h). These data were further supported by RNAscope-based staining for viral RNA combined with LC3 staining, showing that the colocalization of viral RNA and LC3B in WT cells was further enhanced by BafA1, but not in FIP200-deficient cells (Fig. 6i, j). To further characterize the vesicular compartment involved in FIP200-dependent degradation of viral RNA, we carried out sucrose gradient fractionation by ultracentrifugation of lysates from SARS-CoV-2-infected A549-hACE2 WT and FIP200-deficient cells and analyzed for presence of LC3B and viral RNA in each fraction (Fig. 6k). Most of the viral RNA identified in LC3B-positive vesicles localized to one given fraction (Fig. 6l), and this specific fraction was positive for LC3B-II in a FIP200-dependent manner (Fig. 6m, Supplementary Fig. 10b). Taken together, these data demonstrate that the antiviral mechanism of FIP200 is mediated by degradation of virions and viral RNA in LC3B positive acidified compartments generated through a virus-activated non-canonical autophagy pathway, revealing an unconventional function of FIP200 (Supplementary Fig. 10c).

Discussion

In this work, we describe the cellular phenotype of FIP200 deficiency in two unrelated patients with critical COVID-19 pneumonia. Based on characterization of deleterious FIP200 variants from the patients as well as FIP200 KO cells, including a primary pulmonary epithelium cell model, we establish a causal relationship between FIP200 deficiency and susceptibility to SARS-CoV-2 infection. Moreover, we describe a novel antiviral function of the autophagy-related protein FIP200, which exerts cell-autonomous restriction of virus replication by a mechanism independent of canonical autophagy and type I IFN immunity. Based on the data presented, we propose an antiviral mechanism by which SARS-CoV-2 is degraded in acidified single-membrane LC3B-positive compartments by non-canonical autophagy in a FIP200-dependent manner. Collectively, our data suggest that defects in this autophagy-related antiviral pathway impair immunity to SARS-CoV-2 and facilitate development of critical COVID-19 in patients. Our findings also add to the emerging literature on non-redundant roles for innate antiviral mechanisms operating independently of classical type I IFN immunity[67].

The main finding of the present study is the identification of deleterious variants in the *RB1CC1/FIP200* gene in patients with critical COVID-19 and the subsequent discovery of a FIP200-dependent antiviral mechanism involving lysosomal degradation of virions and viral RNA through non-canonical autophagy. These data suggest a pathogenic role of FIP200 deficiency in susceptibility to critical COVID-19. We present evidence based on two unrelated patients with critical COVID-19 with rare monoallelic FIP200 missense variants, including A55V (P1) and R474C (P2), predicted to be deleterious. Both variants are localized in the N-terminal domain of FIP200 in a region important for protein-protein interactions mediating initiation of autophagy and phagophore formation[68,69]. We show impaired LC3B-I to LC3B-II conversion by chemical autophagy inducers and SARS-CoV-2 exposure in patient MdMs. Importantly, primary human pulmonary cell models and A549-hACE2 cells deficient in FIP200 expressing the P2 variant revealed enhanced viral replication and disturbed autophagy flux. Expression of FIP200 was sufficient to promote antiviral activity, and accordingly, reconstitution of FIP200-deficient cell lines with FIP200 lead to improved control of viral replication. The proportion of patients with variants in the N-terminal portion of FIP200 was enriched in the critical COVID-19 patient cohort compared to the general population, and expression of frequent FIP200 haplotypes from gnomAD did not show increased viral replication, suggesting that deleterious FIP200 variants are very rare in the general population. Functional studies of the immunological, virological, and autophagy phenotype of cells from patients with other FIP200 variants will provide further mechanistic details and shed more light on inheritance, penetrance, and clinical phenotype of FIP200 deficiency.

With respect to the FIP200-dependent anti-SARS-CoV-2 effector mechanism, we propose that this is mediated by lysosomal degradation of virions and viral macromolecules, including RNA, through a lysosomal, non-canonical autophagy pathway involving LC3B-II positive single-membrane compartments. These conclusions are based on a series of data. We first established that KO of the essential autophagy protein ATG5 did not cause elevated SARS-CoV-2 replication, thereby arguing against canonical autophagy as the antiviral mechanism of FIP200. In agreement with this, double-membrane autophagosomes did not contain virions or virus-replication-associated cellular structures, as has been previously described for certain viruses and intracellular bacteria[20,70]. Ultrastructural examination of SARS-CoV-2-infected pulmonary A549-hACE2 cells by TEM revealed that cellular

https://doi.org/10.1038/s41467-025-65308-8

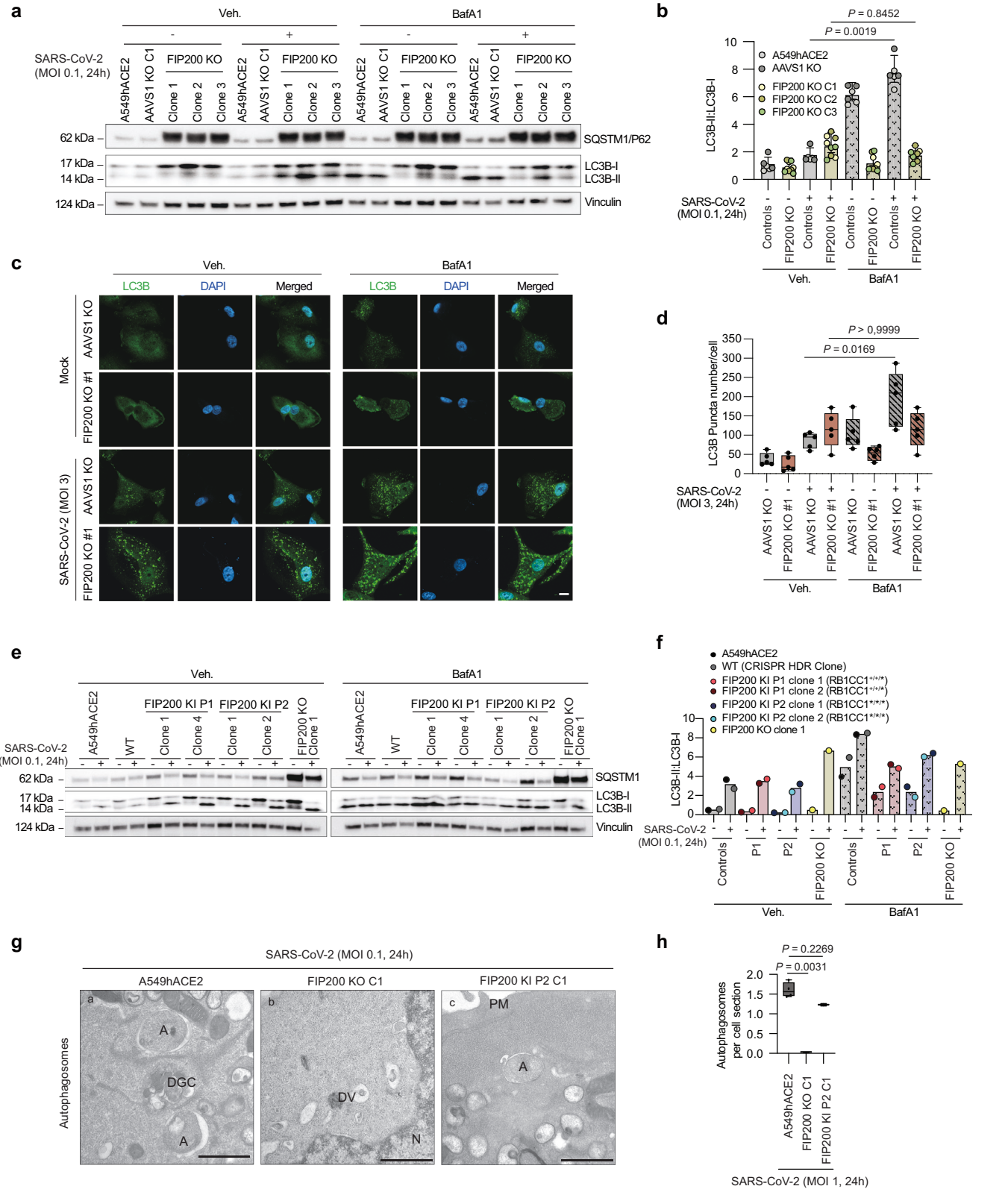

compartments for viral replication, including DMVs, LVCV, and spherules[55], were more abundant in cells with FIP200 deficiency, further underscoring that the absence of FIP200 favors SARS-CoV-2 replication. Importantly, this analysis also uncovered that infected cells contained virions in single-membrane degradative vesicles, and the fraction of these virion-containing degradative compartments was significantly reduced in FIP200-deficient cells. Confocal microscopy of cells stained for LC3B, SARS-CoV-2 RNA, and acidified compartments confirmed that FIP200 promotes formation and delivery of viral RNA into degradative compartments, which are LC3B positive, and also that the infection-induced LC3B-positive vesicle-like structures are virus positive. Finally, subcellular fractionation of eluates from LC3B-immunoprecipitated cell lysates from WT and FIP200 KO cells revealed enrichment of viral RNA in a fraction positive for LC3B-II,

Fig. 4 | FIP200-deficient cells display impaired SARS-CoV-2-induced autophagy flux. a WT, monoclonal AAVS1 clones 1 and FIP200 KO (clones 1–3) A549-hACE2 were infected with SARS-CoV-2 (MOI 0.1, 24 h) with or without 200 nM bafilomycin A1 (BafA1) for 3 h before being lysed for immunoblotting. **b** Quantification of LC3B-II:LC3B-I ratio in (**a**). (mean ± SD; Controls n = 6, FIP200 KO n = 9) **c** Immunofluorescence of polyclonal AAVS1 KO and FIP200 KO (guide #1) hACE2-A549 cells infected with SARS-CoV-2 (MOI 3, 24 h) with or without 200 nM BafA1. Scale bar, 10 μm. **d** Quantification of LC3B-positive puncta per cell shown in (**c**) was analyzed using ICY software (mean ± SD, n = 5, each data point represents the mean value per image). **e** A549-hACE2 WT, monoclonal FIP200 KO clone 1, FIP200 KI P1 clone 1, FIP200 KI P1 clone 4, and FIP200 KI P2 clones 1, FIP200 KI P2 clones 2, and CRISPR HDR knock-in WT were infected with SARS-CoV-2 (MOI 0.1, 24 h) and analyzed by immunoblotting. **f** Quantification of LC3B-II:LC3B-I ratios in (**e**). **g** A549-hACE2 WT, monoclonal FIP200 KO clone 1, and monoclonal FIP200 KI P2 (clone 1) A549-hACE2 cells were infected with SARS-CoV-2 (MOI 1, 24 h) and processed for EM. Autophagosomes in the samples were examined. A autophagosome, DGC degradative compartment, DV dark vacuole, PM plasma membrane, N nucleus. Scale bar, 1 μm. **h** Quantification of autophagosomes per cell section was performed for each condition, 200 randomly selected cell profiles from four independent grids (mean ± SEM, n = 4). Data are representative of three independent experiments (**a**–**f**), **c**, **g** show representative images. Statistical analysis was performed using the Kruskal–Wallis test with two-sided Dunn's multiple comparison correction (**b**, **h**) and One-way ANOVA with two-sided Tukey's multiple comparison correction (**d**). Box plots show median (center line), 25th–75th percentiles (box), and min–max values (whiskers) (**d**, **h**). Source data are provided as a Source data file.

which was absent in FIP200-deficient cells. These data suggest that the observed FIP200-dependent antiviral mechanism relies on non-canonical autophagy, in contrast to previously reported canonical autophagy in xenophagy[20,70].

Our work demonstrates that the FIP200-dependent antiviral pathway is not targeting incoming SARS-CoV-2 as has been proposed previously for other viruses[71,72], but rather a relatively late step in the viral lifecycle. Targeting of later stages of virus replication has been reported for other viruses and other cell types, but in those studies occurring through ATG5-dependent canonical autophagy[20,73]. Our conclusion is based on data showing that elevated levels of virus replication in FIP200-deficient cells were not apparent the first 2 h after infection. This correlates with virus-induced autophagy being dependent on replication. Third, pulse-chase experiments, RNA scope, and fractionation showed that SARS-CoV-2 virions and RNA were localized to degradative vesicles/compartments in productively replicating cells in a FIP200-dependent manner. Therefore, the FIP200-mediated antiviral pathway is not a constitutive immune mechanism conferring an elevated barrier for establishment of infection in individual cells[74], but rather a virus-induced cell-autonomous antiviral pathway limiting replication and production of progeny virions.

In relation to the mechanism that links viral replication to the antiviral degradative pathway, we identified the selective autophagy receptor NDP52 to be a plausible molecule acting in the antiviral FIP200-dependent pathway. Similar to our observations for FIP200, the antiviral effect of NDP52 did not appear to rely on canonical autophagy, in agreement with previous reports and observations with other SARs[75–77]. Rather, NDP52 has been linked to induction of selective autophagy through direct interaction with FIP200, thereby activating the ULK kinase complex[66]. Mechanistically, NDP52 stimulates association of FIP200 to membranes and serves as an important link between autophagy, the ATG machinery and the ubiquitination system, since NDP52 recognizes and binds to autophagic substrates in a ubiquitin-dependent manner[78,79]. Along this line, our data suggest a model whereby NDP52 serves as a SAR recognizing and targeting SARS-CoV-2 virions for degradation in LC3B-positive degradative compartments through interaction with FIP200, although this remains to be further explored. Interestingly, NDP52 also plays an important role in regulating inflammation by degrading numerous immune regulators via autophagy[79,80]. Our data suggest that the NDP52-FIP200 axis is disrupted in FIP200-deficient cells and patient PBMCs, thus explaining the tendency for hyperinflammation observed in response to SARS-CoV-2 infection. Altogether, we propose that, like FIP200, its binding partner NDP52 exerts antiviral activity against SARS-CoV-2, and our data suggest that these two proteins may be connected in the same antiviral pathway against SARS-CoV-2. With the data currently available, however, it remains possible that FIP200 exerts antiviral activity fully or partly independently of NDP52. For instance, it has been shown that FIP200 possesses lysosomal targeting functions unrelated to autophagy for degradation of ferritin[81]. More work is required to clarify this mechanistically.

The antiviral activity of FIP200 described in the present study is unlikely to be mediated via type I IFNs or inflammatory cytokines, although FIP200 has been reported to promote RIG-I signaling[82]. In the experimental pulmonary cell models used as well as in patient PBMCs, we found that FIP200 deficiency did not impair induction of type I and III IFNs and ISGs. Indeed, we consistently observed similar or even enhanced type I IFN and cytokine responses in FIP200 KO compared to WT cells. Several mechanisms may account for this observation. First, enhanced viral replication may lead to secondary increases in type IFN and cytokine production. Second, the reduced autophagy activity may release the negative modulatory effect of ATG proteins and autophagy upon signaling by PRRs and inflammatory cytokine and type I IFN pathways, as previously reported in relation to RLR and cGAS/STING pathways, as well as in inflammasome activation[83–85]. Taken together, these data support the rest of our results and argue for a cell-autonomous mode of antiviral activity by FIP200. It should be noted, however, that autophagy also plays an important role in antiviral immunity in the adaptive immune system[34], and we cannot exclude that FIP200 deficiency and the patient variants in FIP200 may have implications beyond the innate cell intrinsic system investigated here.

The importance of autophagy processes in regulation of cellular homeostasis, inflammation, metabolism, and cell death has been highlighted by seminal work establishing definitive etiological links between variants in genes that control autophagy and human disease, particularly neurodegenerative conditions, inflammatory disorders, and cancer[34]. From a medical perspective, the evidence provided here, as well as by others[86,87] of autophagy-related pathways and ATG proteins exerting a putative key antiviral role against SARS-CoV-2, may have important medical implications. These insights suggest that IEI in genes encoding and regulating ATG proteins or other autophagy-related processes should be searched in patients with critical COVID-19 or other severe presentations of SARS-CoV-2 infection. At present, no IEI related to FIP200 function in autophagy or beyond has been reported. However, it is important to note that homozygous FIP200 deficiency is lethal in mice, whereas heterozygous FIP200 deficiency causes neonatal lethality, because the newborn mice require autophagy to survive the starvation period until lactation is established[88,89]. Given the essential role of FIP200 in mammals, it appears unlikely that humans homozygous for complete loss-of-function variants will survive. Results of the present study suggest that monoallelic, partial defects in ATG proteins may cause increased risk of viral infection and some degree of immune dysregulation. This idea is in line with previous publications linking IEI affecting ATG genes to severe viral infection, including deleterious variants in *ATG4A* and *LC3B2* in patients with recurrent lymphocytic Mollaret meningitis[42], a variant in *ATG7* in poliomyelitis[43], and a dominant negative TBK1 variant causing defective cGAS-induced autophagy in a patient with herpes simplex virus encephalitis[44]. These reports, together with the present study, demonstrate medically relevant implications of defective canonical and non-canonical autophagy-related processes for antiviral immunity in humans, prompting the search for gene variants in these pathways in

https://doi.org/10.1038/s41467-025-65308-8

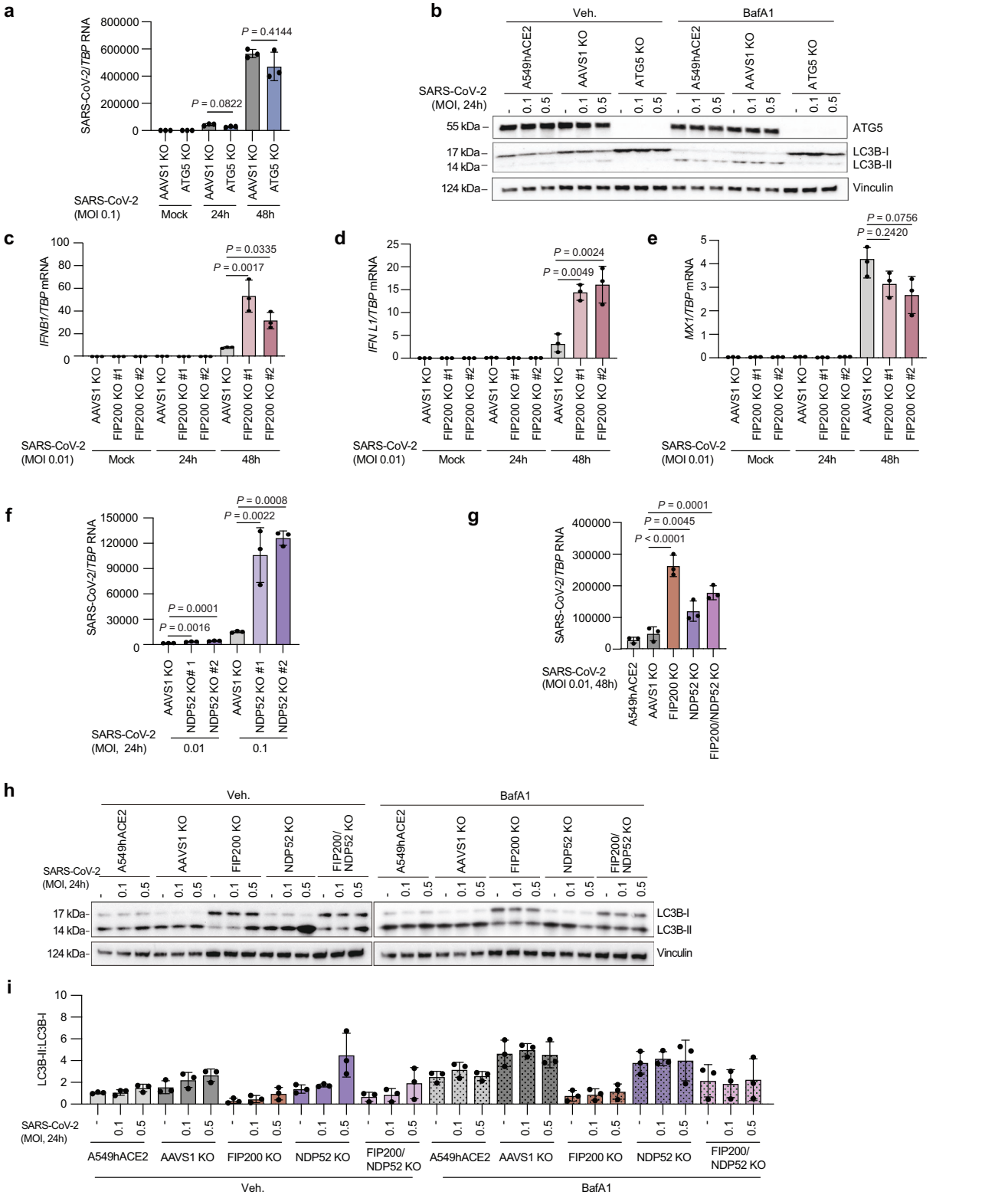

patients with severe viral infections and possibly inflammatory disorders.

Collectively, this study describes a novel cell-autonomous antiviral function of FIP200 against SARS-CoV-2 in human pulmonary cells through a degradative non-canonical autophagy pathway leading to (endo)lysosomal degradation of virions in LC3B-positive acidified vesicles. We suggest that autophagy-related gene variants in patients might represent an IEI predisposing to severe SARS-CoV-2 infection, and specifically that deleterious variants in FIP200 increase susceptibility to critical COVID-19. Future identification and characterization of defects in other autophagy-related genes will likely help to further decipher the molecular pathways underlying antiviral properties of autophagy-related processes. This approach will broaden the understanding of innate antiviral restriction mechanisms and their

Fig. 5 | The antiviral activity of FIP200 is independent of canonical autophagy and IFN, and involves NDP52. a, **b** Polyclonal AAVS1 KO and polyclonal ATG5 KO A549-hACE2 cells were infected with SARS-CoV-2 at the indicated MOI for 24 and 48 h, as indicated. **a** Total RNA was isolated and analyzed for SARS-CoV-2 RNA by RT-qPCR. Data were normalized against TBP (n = 3). **b** ATG5 or vinculin levels in cell lysates were evaluated by immunoblotting. **c**–**e** polyclonal FIP200 KO (guide #1 and #2) and polyclonal AAVS1 KO cells were infected with SARS-CoV-2 at an MOI of 0.1. Total RNA was extracted from cells at 24 and 48 h p.i., and *IFNB1*, *IFNL1*, and *MX1* mRNA levels were measured by RT-qPCR. Data were normalized against TBP (n = 3). **f**–**i** Polyclonal AAVS1 KO and polyclonal NDP52 KO (guide #1 and #2) A549-hACE2 cells (**f**) or Polyclonal AAVS1 KO, polyclonal FIP200 KO, and FIP200/NDP52 double KO A549-hACE2 cells were infected with SARS-CoV-2 at the indicated MOIs for 24 or 48 h as shown. Total RNA was isolated, and SARS-CoV-2 RNA was measured by RT-qPCR. Data were normalized against TBP (n = 3). **h** Cell lysates were collected and analyzed by immunoblotting. **i** Ratios of LC3B-II to LC3B-I in the experiment shown in (**h**) were quantified by densitometry (n = 3). All data are representative of three independent experiments. Quantifications are shown as mean ± SD, statistical analysis was carried out using two-sided Student's t test with Bonferroni multiple comparison correction (**a**) and One-way ANOVA with two-sided Dunnett's multiple comparison correction (**c**–**g**). Source data are provided as a Source data file.

physiological relevance beyond the type I IFN system. Uncovering the antiviral mechanism of FIP200 may also facilitate the development of novel strategies for the treatment of infections by coronaviruses and other emerging viruses. Finally, identification and investigation of individuals carrying such gene variants can be translated into personalized medicine to prevent severe disease from SARS-CoV-2 or related viruses through vaccination, antiviral prophylaxis, or intensified treatments, while at the same time providing insights into fundamental protective antiviral signaling pathways in human immunology.

Methods

Patient material

The patients included in this study are part of a larger cohort study on patients <60 years, without significant comorbidities and with severe or critical COVID-19 (WHO category IV and V) admitted to a hospital intensive care unit and receiving oxygen (>5 L) or ventilatory support. Patients with co-morbidity, including age > 60 years, pulmonary or cardiovascular disease, diabetes, BMI > 30, pregnancy, malignancy, or known primary or secondary immunosuppression (including immunomodulating therapies) were excluded.

Whole blood was first collected at hospitalization in either EDTA-stabilized tube for DNA isolation or in lithium heparin tubes for peripheral blood mononuclear cells (PBMCs) isolation. PBMCs were isolated by Ficoll density gradient centrifugation using SepMate PBMC isolation tubes (Stemcell Technologies, # 86460) and frozen in liquid nitrogen. Control PBMCs were purified from healthy donors after obtaining a written consent. Genomic DNA from the isolated PBMCs was purified using the QIAamp DNA Blood Mini kit (Qiagen, 69,504) according to manufacturer's instructions. Monocyte-derived macrophages (MdMs) were differentiated from 5×10^5 PBMCs in RPMI containing 10% heat-inactivated fetal calf serum (HI-FBS), 10% human AB serum (Sigma-Aldrich, H4522), 10,000 IU/ml penicillin/streptomycin (P/S; Sigma-Aldrich, 15140122), and 15 ng/ml human CSF1/M-colony stimulating factor 1 (CSF1) (Peprotech, 300–25). Medium was changed to DMEM (Biowest, L0102) with 10% human AB serum, 15 ng/ml CSF1 on days 4 and 7. The MdMs were used for experiments on day 9.

Whole-exome sequencing (WES) and bioinformatics

Genomic DNA was isolated from whole blood from each patient as previously described[90,91]. WES was performed employing the Kapa HTP Library preparation and the Nimblegen SeqCap EZ MedExome Plus kit (Roche, 07681364001) for P1 and TWIST comprehensive exome with custom spike-ins for P2. Samples were analyzed on Illumina NextSeq 550 system (P1) and NovaSeq 6000 (P2), SNP calling relative to hg19 with BWA, PCR, and optical duplicates were identified and marked. The alignment was recalibrated using the GATK package. Single-nucleotide polymorphisms were identified employing the HaplotypeCaller from the GATK package. Variant call files were analyzed and filtered using VarSeq 2.3.0 (Golden Helix) or Tibco Spotfire Analyst and filtered according to confidence (call quality at least 30.0, read depth at least 5.0, allele fraction at least 25.0). We then used different variant scoring systems, including combined annotation-dependent depletion (CADD), mutation significance cut-off (MSC), gene damage index (GDI), SIFT, and PolyPhen-2, to identify variants of interest. The exomes were analyzed for deleterious variants using a CADD score >20 and a frequency below 0.001 in the general population based on frequencies reported to the Genome Aggregation Database (gnomAD), ExAC, and NHLBI ESP. Finally, identified variants were manually checked by inspecting BAM files using IGV.

Amino acid sequence alignment

The following FIP200 sequences were obtained from UniProt [http://www.uniprot.org/]: Homo sapiens Q8TDY2, Mus musculus Q9ESK9, Pan troglodytes H2QW57, Molossus molossus A0A7J8DUJ3, Pongo abelii H2PQA4, Callithrix jacchus U3BY99, Myotis myotis A0A7J7TJ49, Phyllostomus discolor A0A6J2M766, Caretta caretta UPI0020947A0F, Hylobates moloch UPI0013F1E6E8, Macaca mulatta F6QUC5, Pipistrellus kuhlii UPI00174ED5F7, Nomascus leucogenys G1QJA4.

Cell lines

Human lung adenocarcinoma epithelial A549 cells expressing human ACE2 (A549-hACE2), kindly provided by Brad Rosenberg (Icahn School of Medicine, Mount Sinai, New York, USA), and VeroE6 cells expressing human TMPRSS2 (VeroE6-hTMPRSS2), kindly provided by Stefan Pöhlmann (University of Göttingen, Germany). These cell lines were not newly established from primary human or animal tissues. The sex of the donor for these cell lines is not known. All cell lines were routinely tested for mycoplasma contamination and cultured under recommended conditions as described in the following. Cells are maintained in Dulbecco's modified Eagle's medium (DMEM, Biowest, L0102). The medium was supplemented with 10% HI-FCS and 10,000 IU/ml P/S. The Vero E6-TMPRSS2 cell culture medium was additionally supplemented with 10 µg/ml blasticidin (Invivogen, A1113903) to maintain the TMPRSS2 expression plasmid. All cell lines were incubated at 37 °C with 5% CO_2.

Air–liquid interface pulmonary epithelium model

Cells were collected, cultured, differentiated, maintained, infected with virus, and harvested from membranes as previously described[24]. In brief, primary nasal cells were isolated using a nasal brush (Dent-O-Care). Cells were cultured as a monolayer in tissue culture flasks coated with 0.1 mg/ml of bovine type I collagen solution. At passage two, cells were seeded at $2–3 \times 10^4$ cells on 6.5 mm Transwell membranes (Corning, 3470) coated with 30 µg/ml of bovine type I collagen solution and submerged in 2 × P/S (200 U/ml) DMEM-low glycose (Sigma-Aldrich, D5921) mixed 1:1 (v/v) with 2× Monolayer medium (Airway Epithelium Cell Basal Medium, (PromoCell C-21260), supplemented with 2 packs of Airway Epithelial Cell Growth Medium Supplement, (PromoCell, C-39160), without triiodothyronine and conatain 1 ml of 1.5 mg/ml bovine serum albumin). When cultures reached confluency, air–liquid interface was introduced, and medium changed to ALI medium (Pneumacult ALI medium kit [StemCell, 5001]) with ALI medium supplement [StemCell, 5001] containing 100 U/ml P/S, 0.48 µg/ml hydrocortisone [StemCell, 07925], and 4 µg/ml heparin [StemCell, 07980]. Cells were allowed to differentiate for at least 21 days, as verified by extensive cilia beating and mucus covering, prior to experiment initiation.

https://doi.org/10.1038/s41467-025-65308-8

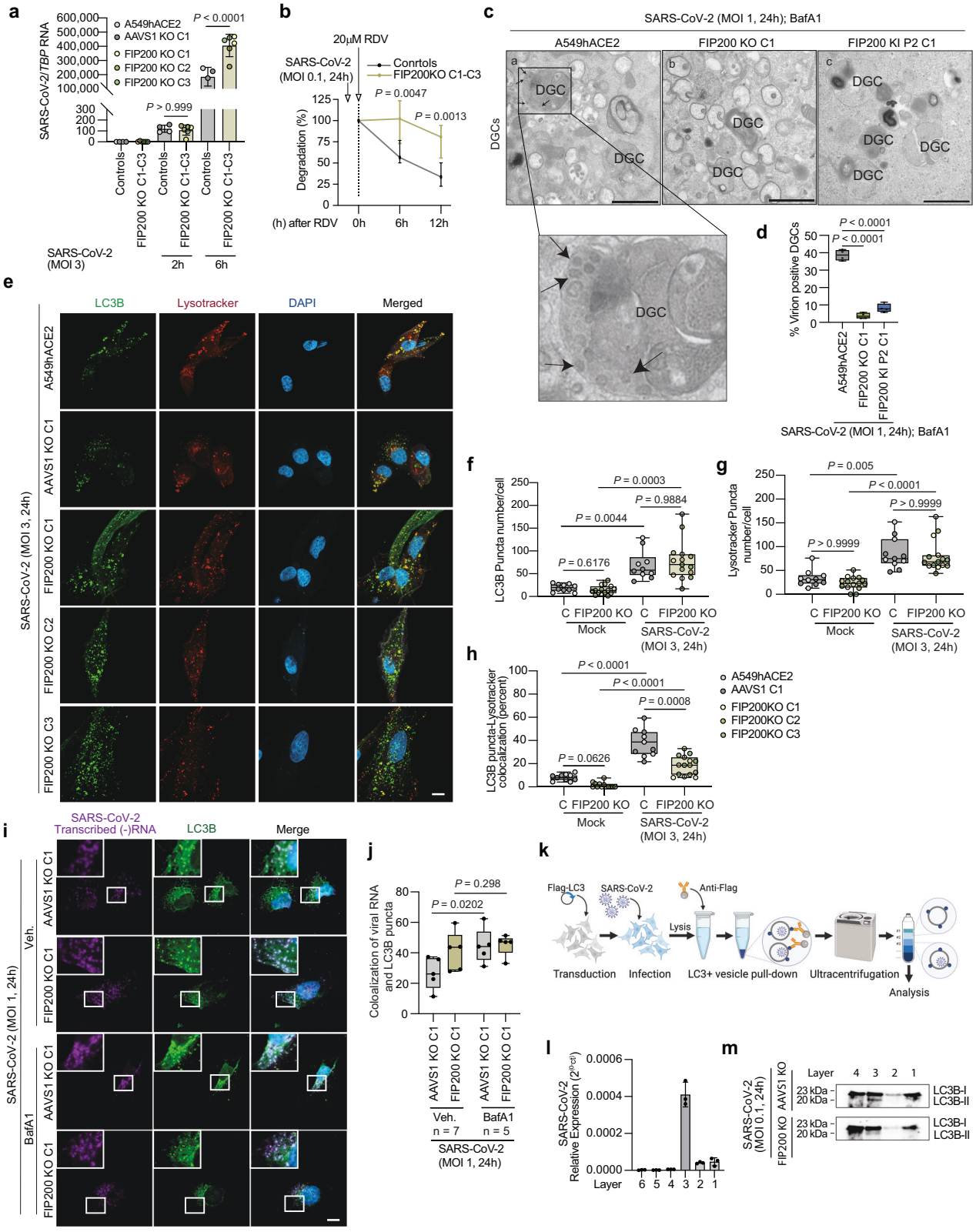

Virus and propagation

The SARS-CoV-2 B.1 isolate, a Wuhan-like early European variant isolated in Freiburg clone 4286, was generously provided by Georg Kochs (University of Freiburg, Germany). The SARS-CoV-2 alpha (B.1.1.7) variant was kindly provided by Arvind Patel (University of Glasgow, United Kingdom). Alex Sigal (African Health Research Institute, Durban, South Africa) kindly provided the SARS-CoV-2 beta (B.1.351) and Omicron (B.1A) variants. The SARS-CoV-2 delta (B.1.617.2) variant was obtained from the Danish State Serum Institute in Copenhagen (Denmark). The isolates were sequenced within 1–2 passages after initial propagation, and the corresponding sequences are available as follows: Freiburg, FR-4286 (GISAID accession no. EPI_ISL_852748), B.1.1.7 (NCBI GenBank accession no. MZ314997), B.1.351 (GISAID accession no. EPI_ISL_678615), and

Fig. 6 | FIP200 targets SARS-CoV-2 for degradation in acidified lysosomal single-membrane compartments. a RT-qPCR of SARS-CoV-2 (MOI 3) infected cells at indicated time points. Data normalized to TBP (Controls n = 4, FIP200 KO n = 6). **b** WT and FIP200 KO cells were infected (MOI 0.1, 24 h), then treated with remdesivir (RDV, 20 mM) for the additional time and analyzed by RT-qPCR and normalized to TBP (n = 3). **c** WT, monoclonal FIP200 KO (clone 1), FIP200 KI P2 (clone 1) A549-hACE2 cells were infected (MOI 1, 24 h) and treated with BafA1 3 h before EM; Arrows point to virions in DGCs; DGC degradative compartment; Scale Bar, 1 μm. **d** Quantification of virion-containing DGCs. Quantifications were performed by examining 200 randomly selected cell profiles from four independent grids (mean ± SEM, n = 4). **e** Immunofluorescence staining of control and FIP200 KO cells (MOI 3, 24 h). Scale bar, 10 μm. Quantification of LC3B-positive puncta per cell (**f**), Lysotracker puncta per cell (**g**), and percentage of LC3B-positive puncta-Lysotracker colocalization (**h**) by ICY software (Controls n = 10, FIP200 KO n = 15). **i** SARS-CoV-2 (-sense) RNA and LC3B puncta were visualized by RNA Scope and anti-LC3B staining. Scale bar, 10 μm. **j** Quantification of colocalization of SARS-CoV-2 RNA and LC3B-positive puncta was analyzed by ICY software(n = 5). **k** Schematic illustration of the experimental procedure for (**l**, **m**). Created in BioRender. Paludan, S. (2025) https://BioRender.com/xu0qpxw. **l** RNA from 6 ultracentrifugation fractions was measured by RT-PCR. Data shown as relative levels (n = 3). **m** Ultracentrifugation fractions were analyzed by immunoblotting. Data are representative of three independent experiments (**a**, **b**, **e**–**m**), **c**, **e**, **i** show representative images. Each data point represents the mean value per image (**f**–**h**, **j**). Quantification except (**d**) shown as mean ± SD. Statistical analysis: one-way ANOVA, two-sided Tukey (**a**, **d**), unpaired Welch's t test, two-stage linear step-up (**b**), Brown-Forsythe Welch ANOVA tests, two-sided Dunnett's T3 (**f**, **h**), Kruskal–Wallis test, two-sided Dunn's (**g**), and two-sided Mann–Whitney test, Bonferroni (**j**). Box plots show median (center line), 25th–75th percentiles (box), and min–max values (whiskers) (**d**, **f**–**h**, **j**). Source data are provided as a Source data file.

B.1.617.2 (SARS-CoV-2/DK/SSI-H11, NCBI GenBank accession no. OM444216).

Virus propagation was conducted in VeroE6 cells expressing hTMPRSS2. Briefly, 10×10^6 cells were seeded in 6 ml of medium in a T175 culture flask (Thermo Fisher Scientific, 156505) and infected at a multiplicity of infection (MOI) of 0.05. At 1 h post-infection, the culture medium was increased to a total volume of 12 ml, and virus propagation continued for up to 72 h or until a cytopathic effect (CPE) of approximately 70% was observed. To harvest the virus, the cell culture supernatant was collected, centrifuged at $300 \times g$ for 5 min to eliminate cellular debris, before further concentration by centrifugation at $4000 \times g$ for 25 min using a 100 kDa filter (Amicon, 36100101). The concentrated virus was aliquoted and stored at −80 °C. The infectious virus titer in the generated stocks was determined using a limiting dilution assay[92].

Infection assays (and reagents)

A549-hACE2 cells at a concentration of 24×10^4 were seeded in a 12-well in 1 ml of DMEM, supplemented with 10% hi-FCS, 2 mM L-glutamine, 100 U/ml penicillin, and 100 μg/ml streptomycin. The following day, cells were infected with SARS-CoV-2 at an MOI as indicated in each individual experiment. Infections were performed in DMEM with 2% fetal calf serum (FCS) for 1 h, after which unbound virus was removed by washing the cells with Dulbecco's Phosphate Buffered Saline (PBS, Sigma-Aldrich, 32129211). Cells were subsequently cultured in 1 ml of DMEM for 24 or 48 h before collecting cell culture supernatants and cells. Supernatants were stored at −80 °C until further analysis by ELISA, MSD, or limiting dilution assay, while the cells were washed with PBS and processed for western blot analysis or qPCR. Infection of ALI cells was performed as previously described[24]. Cells were infected with SARS-CoV-2 at an MOI as indicated in each individual experiment. To infect cells, 100 μl DMEM-low glycose with or without virus was added to the apical compartment and left in a 37 °C incubator for 1 h. Following this infection, all liquid was removed from the apical compartment, and membranes were placed in an incubator at 37 °C, 5% CO_2 for 72 h before collecting cell culture supernatants and cells. Supernatants were stored at -80 °C until further analysis. Specific inhibitors such as Ritonavir (Sigma-Aldrich, SML0491), Lopinavir (Sigma-Aldrich, SML1222), cycloheximide (Sigma-Aldrich, 01810), Remdesivir (InvivoGen, 469411000), and bafilomycin A1 (Sigma-Aldrich, SML1661) were used in determined experiment at the indicated concentrations. Autophagy was induced by starving cell in EBSS (Gibco, 14155048). For mouse experiments, transgenic K18-hACE2 C57BL/6J mice (strain: 2B6.Cg-Tg(K18-ACE2)2Prlmn/J, The Jackson Laboratory, Stock number: 034860, Maine, USA) expressing human ACE2 were used. Age-matched male and female mice (8–12 weeks old) were randomized into experimental groups. Mice were housed in a specific pathogen-free facility under controlled conditions (12-h light/dark cycle, ambient temperature of 20–24 °C, and relative humidity of 40–60%) and fed a standard chow diet with water ad libitum. For infection, mice were anesthetized with isoflurane and intranasally inoculated with 1.5×10^3 plaque-forming units (PFU) of B.1.1.7 SARS-CoV-2 (Kent, UK isolate). At day 6 post-infection (p.i.), lungs were collected and homogenized in 1 ml PBS for downstream analysis[93].

Limiting dilution assay

The limiting dilution assay was employed to determine the amount of infectious virus in cell culture supernatants or generated virus stocks. 2×10^4 VeroE6-hTMPRRS2 cells were seeded in a 96-well plate in 50 μl DMEM. The next day, supernatants or virus stocks were thawed and diluted five times, followed by 10-fold serial dilution using DMEM, before adding 50 μl of each dilution to the cells. The final dilution range was 10-1 to 10-11, in quadruplicate for supernatants or octuplicate for virus stocks. Each well was evaluated for CPE using a standard light microscope, and the tissue culture infectious dose 50 (TCID50/ml) was calculated using the Reed and Muench method[92]. The TCID50/ml values were multiplied by factor 0.7 to convert them into the mean number of plaque-forming units (PFU)/ml (ATCC – Converting TCID50 to PFU).

Generation of polyclonal knockout A549-hACE2 cells by CRISPR/Cas9 editing

FIP200 (*RB1CC1*), *ATG5*, *NDP52* (*CALCOCO2*), and *FAM134B* polyclonal knockout (KO) cell lines were generated using the CRISPR/Cas9 gene editing technology. Briefly, ribonucleoprotein (RNP) complexes were generated by incubating 1.2 μg of Cas9 protein (Integrated DNA Technologies, 10000735) with 2 μg of sgRNA at room temperature for 15–20 min. Then 100,000–200,000 cells were washed with PBS, resuspended in 20 μl of OPTI-MEM (Thermo Fisher Scientific, 31-985-070), mixed with the RNP complexes, and transferred into a Nucleocuvette strip chamber (Lonza). Nucleofection was then performed using the Lonza 4D-NucleofectorTM System (program CM138) and cells were subsequently cultured for 7–21 days as described above. The KO efficiency was determined by both western blotting and DNA sequencing. The sequences of the synthetic guide RNA used for the KO were purchased from Synthego and are as follows: FIP200#1: CUCCAUUGACCACCAGCACC; FIP200#2: CAAGAUUGCUAUUCAACACC; ATG5: CCUUAGAUGGACAGUGCAGA; FAM134B: GCCACTGTATTGCAGAATCA; NDP52#1: ACUUCUUGUCAUUGCAGGUG; NDP52#2: UCUUGUCAUUGCAGGUGGGG; and AAVS1 (control sgRNA): GGGGCCACTAGGGACAGGAT[94]. Monoclonal FIP200 KO were generated from polyclonal FIP200 KO. Briefly, the polyclonal FIP200 KO cells were seeded in the 96-well plate in the ration of 0.3 cell/well, and cells maintained in DMEM medium supplemented with 10% HI-FCS 10,000 IU/ml P/S for 1- or 2-month, and fresh medium was changed every 2 weeks. Monoclonal FIP200 KO clones were verified by both western blotting and DNA sequencing.

Generation of knock-in ACE2-A549 by CRISPR/Cas9 editing

To generate the monoclonal knock-in (KI) ACE2-A549 cell clones, 2×10^5 A549-ACE2 cells were nucleofected as described above with Cas9 RNPs (125 pmol Cas9-150 pmol crRNA:tracR duplex) and 5 μM of HDR-Donor DNA oligo, before to transferred to prewarmed medium containing 1 μM HDR Enhancer V2 (Integrated DNA Technologies, 10007910). After 24 h, the medium was changed, and cells were expanded for 72 h before plating single-cell clones by limiting dilution. Single KI cell clones with successful HDR were identified by Sanger Sequencing. For each HDR edit, cRNA, HDR-donor ssDNA oligo, and genotyping primers (all purchased from Integrated DNA Technologies, IDT) are listed consecutively:

A55V: crRNA_FIP200_A55V (IDT Alt-R crRNA): GGTCAATGGAGGAGAATGCA, HDR_Donor_A55V: ATACAAGATTGCTATTCAACACCAGGTGCTGGTGGTCAATGG***C***GGAGA***G***TGCATGGCTG**T**AGAT CGAAGAGTGTGTACCTACAGTGCTGGGACGGTAGGT, genomicPCR_A55V_fw: GGAATAGCAGGTGGACGATCA, genomicPCR_A55V_rev:AGCCTGAGGATTTTAATAGACCT, A55V_seqPrimer: TGGACGATCACATAAGATCATTTC; R474C: crRNA_FIP200_R474C (IDT Alt-R crRNA): CTAACAGCTCTATTACGAGG, HDR_Donor_R474C:TCATGCTGATCAAGATG GAGAGAAGTTACAAGCTTTGCTC**T**GCCT***G***GTAATAGAGCT***C***TTAGAA AGAGTCAAAATTGTTGAAGCTCTTAGTACAGTTCCT, genomicPCR_R474C_fw: TGTCAGACTGAAGTAAGTGATTCAT, genomicPCR_R474C_rev: TTGACTAAAGCACCAGCCCA, R474C_seqPrimer: TTTCTCCCAAATGATGGAGTGA; D211N: crRNA_FIP200_D211N (IDT Alt-R crRNA): CAGAGAATGTTTGGGAAGAC, HDR_Donor_D211N: GAGTGCCTAACCAGACATAGTTACAGAGAATGTTTGGGAAGACTG**A**ATTCTTTACC TGAACATGAAGACTCAGAAAAAGCTGAGATGAAA, genomicPCR_D211N_fw: CCCTGCTCATAGAATCAAAGCAC, genomicPCR_D211N_rev: GGGTTAACGATAGCCTCTCTCTG, D211N_seqPrimer: CACTTCCTGACCAAAGATTCCA; T234M: crRNA_FIP200_T234M (IDT Alt-R crRNA): GACGAAAAGATCCACTGAAC HDR_Donor_T234M: TAGTTGTTCTAGGCATATCAGGAGAGAGCACCAGTTCAGT***C***GA***C***CTTTTC**A**TCT CAGCTTTTTCTGAGTCTTCATGTTCAGGTAAAGAAT, same genomic PCR primers as for D211N.

N = coding mutation, ***N*** = silent mutations in crRNA target to prevent recutting of edited locus (where necessary). The generated cell lines were called FIP200 KI P1, FIP200 KI P2, FIP200 D221N, and FIP200 T234M A549-hACE2 cells, respectively.

Lentiviral expression of FIP200 variants in FIP200 KO ACE2-A549 cells

For the reconstitution of FIP200 expression, the FIP200 KO cells were transduced by lentivirus packaged with the pLV-FIP200 WT or the pLV-GFP construct, which were generated and packaged by VectorBuilder. Lentiviral vectors were produced by standard calcium phosphate transfection of the packaging plasmids pMD2.G, pRSV-Rev, and pMDlg/pRRE together with either pLV-FIP200 WT or pLV-GFP into HEK293T cells. After 48 h of transfection, virus-containing supernatants were collected, filtered through 0.45-μm filters, and added to FIP200 KO A549-hACE2 cells, which were seeded at 1×10^5 cells per well in a 6-well plate 1 day prior to transduction. Following selection with 1 μg/ml puromycin, the transduction efficiency was assessed through immunoblotting analysis.

DNA extraction and PCR

To verify the genetic changes introduced using the CRISPR-Cas9 system, cells were harvested, and DNA was extracted using the DNeasy Blood & Tissue kit (Qiagen, 69504). Amplicons were generated using 100 ng DNA as template in a final volume of 40 μl, including 8 μl of 5x Phusion GC buffer (from the Phusion High-Fidelity DNA Polymerase set, Thermo Fisher Scientific, F-530XL), 0.8 μl of dNTPs (100 mM dNTP Set, InvivoGen, 10297018), 0.4 μl of Phusion Green High-Fidelity DNA polymerase (Thermo Fisher Scientific, F534S), 2 μl of 10 μM fw primer and 2 μl of 10 μM rev primer, in an Arktik Thermal Cycler (Thermo Fisher Scientific) using the following program: 1 min at 98 °C; 35x (10 s at 98 °C; 30 s at 68 °C; 1 min at 72 °C); 10 min at 7 °C; indefinitely at 4 °C. The following primers (all purchased from Integrated DNA Technologies, IDT) were used: *RB1CC1* fw: 5′-GGAATAGCAGGTGGACGATCA-3′; *RB1CC1* rev: 5′-AGCCTGAGGATTTTAATAGACCT-3′; Amplicons were separated on a 1% agarose gel using the FastDigest Green Buffer (Thermo Fisher Scientific, B64) before to excise the appropriate bands and purify them using the E.Z.N.A Extraction kit (Omega Bio-Tek, D2500-02), according to manufactures' instructions. Isolated amplicons (60 ng) were finally sequenced and the results analyzed using the Interference of CRISPR Edits online tool (ICE, Synthego).

Reverse transcriptase-quantitative PCR (RT-qPCR)

RNA isolation and qPCR was carried out using the High Pure RNA Isolation kit (Roche, 11828665001) and Applied Biosystems TaqMan RNA to CT One Step kit (Thermo Fisher Scientific, 4392938), respectively, as described by the manufacturers and with the following primers from Applied Biosystems: SARS-CoV-2 NC (forward primer: AAATTTTGGGGACCAGGAAC; reverse primer: TGGCACCTGTGTAGGTCAAC); probe primer: FAM-ATGTCGCGCATTGGCATGGA-BHQ, TBP (Hs00427620_m1), IFNB1 (Hs01077958_s1), IFNL1 (Hs00601677_g1), MX1 (Hs00895608_m1), IFIT1 (Hs03027069_s1), TNFA (Hs00174128_m1) and IL6 (Hs00174131_m1). The mRNA level of each gene was normalized by that of TBP using the formula 2Ct(TBP) −Ct(mRNA X). The resulting normalized ratios are presented in the figures.

Western blotting

Cells were seeded in complemented DMEM, incubated overnight, and treated with the different drugs and/or infected with SARS-CoV-2 following the procedure described in the "Infection assays" section. Cells were washed with ice-cold PBS and lysed in Ripa buffer (Thermo Fisher Scientific, PI8990) supplemented with Complete Ultra protease inhibitor (Sigma-Aldrich, 5892953001) and Benzonase Nuclease (Sigma-Aldrich, E1014-25KU) for 15 min on ice before to be stored at −20 °C. Samples were thawed on ice, diluted 1:1 (v/v) with Laemmli sample buffer (Sigma-Aldrich, 1610747), boiled at 95 °C for 4 min, cooled on ice for 5 min, and loaded together with a Precision Plus Protein™ Dual Color Standards (Bio-Rad, 1610374) onto a 18 well 10% Criterion TGX Precast Midi Protein Gel (Bio-Rad, 5671094) and separated in the Nu PAGE MOPS SDS running buffer (Thermo Fisher Scientific, NP000102). Proteins were subsequently transferred onto a Trans-Blot Turbo Midi PVDF Transfer membrane (Bio-Rad, 1704157) using the Trans-Blot Turbo Transfer System (Bio-Rad). Membranes were washed using TRIS-buffered saline (TBS, Thermo Fisher Scientific, J60764.K2) supplemented with 0,05% Tween 20 (Sigma-Aldrich, P1379) (TBS-T), blocked for 1 h at room temperature in 5% skimmed milk powder (Sigma-Aldrich, 70166) in TBS-T, washed with TBS-T, incubated overnight at 4 °C with any of the primary antibodies diluted in TBS-T containing 5% bovine serum albumin fraction V (Sigma-Aldrich, A7906). Primary antibodies were anti-FIP200 (1:1000 dilution, Cell Signaling technology, D10D11, Rabbit mAb #12436); anti-LC3B (1:1000 dilution, Cell Signaling Technology, Antibody #2775); anti-SQSTM1 (1:1000 dilution, Cell Signaling, D1Q5S, Rabbit mAb #39749); anti-SARS-CoV-2 NC protein (1:1000 dilution, Cell Signaling Technology, HL344, Rabbit mAb #26369); anti-NDP52 (1:1000 dilution, Cell Signaling Technology, D1E4A, Rabbit mAb #60732), anti-ATG5 (1:1000 dilution, Cell Signaling Technology D5F5U, Rabbit mAb #12994) and anti-vinculin (1:1000 dilution, Cell Signaling Technology, E1E9V, Rabbit mAb #13901). After three washes with TBS-T, secondary antibodies were added to the membrane in TBS-T containing 2% skimmed milk powder for 1 h at room temperature. Secondary antibodies were peroxidase-conjugated F(ab)2 donkey anti-mouse IgG (1:10000 dilution, Jackson ImmunoResearch, 715-036-150) or anti-rabbit IgG

(1:10000 dilution, Jackson ImmunoResearch, 711-035-152). Finally, membranes were washed three times and developed using the SuperSignal West Pico PLUS chemiluminescent substrate (Thermo Fisher Scientific, 34095) in a Chemidoc Imaging system (Bio-Rad). Specific bands were quantified by densitometry using the Image J software[95]. All primary antibodies used in this study were validated by the manufacturers, as stated in the product datasheets.

Viral degradation kinetics and inhibitors

Cells were seeded in complemented DMEM, incubated overnight, and infected with the SARS-CoV-2 at MOI 0.1 for 24 h; afterward, cells were treated with 20 µM Remdesivir (RDV; Invivogen, GS-5734) every 8 h. The cells were collected at the indicated time points for further analysis.

Protein determination in supernatants by Mesoscale

Supernatants were thawed at room temperature or 4 °C and, if required, inactivated by adding 1:1 (v/v) 0.4% Triton X-100 (Sigma-Aldrich, 9036-19-5). Expression of IFNs (IFNα2a, IFNβ, and IFNγ) and proinflammatory cytokines (TNFα) was measured in cell culture supernatants using the U-PLEX assays (Meso Scale Diagnostics) according to manufacturer's protocols on a Meso Quickplex SQ 120 instrument[87]. Measurements below the detection limit were not excluded and are indicated with an asterisk (*) in the Source data file.

Immunofluorescence microscopy

Cells were seeded on coverslips and treated as indicated. For experiments involving lysosomal staining, cells were incubated with LysoTracker (1:10,000 dilution; Thermo Fisher Scientific, L12492) for 30 min or Bodipy (2 µg/ml; BODIPY™ 493/503, D3922) prior to fixation. Cells were fixed with 4% paraformaldehyde (PFA) for 15 min at room temperature, followed by three washes with cold PBS. Subsequently, cells were permeabilized by incubation in cold methanol for 5 min at −20 °C. After fixation, cells were blocked in PBS containing 3% fetal calf serum (FCS) for 1 h, followed by overnight incubation with primary antibodies. Primary antibodies were anti-LC3B (1:500 dilution, Nordic Biosite, ARG43536), anti-SQSTM1/p62 (1:200 dilution, Progen, 71001), anti-SARS-CoV-2 S (1:300 dilution, GeneTex, GTX632604), and anti-LAMP-1 (1:300 dilution, Invitrogen, MA1-164). The next day, cells were incubated with secondary antibodies (all Alexa Fluor-conjugated, 1:500 dilution; Invitrogen) for 1 h. Coverslips were mounted on slides using DAPI-containing ProLong Diamond Antifade Mountant (Thermo Fisher Scientific). All primary antibodies used in this study were validated by the manufacturers, as stated in the product datasheets. Z-stack images were acquired using a Zeiss LSM 780 confocal microscope, and orthogonal projection images were processed with Zen Blue software (Zeiss). Data analysis was performed with the ICY software (BioImage Analysis Lab at Institut Pasteur and licensed under GPLv3)[96].

RNAscope

All procedures were performed according to the protocol provided by Advanced Cell Diagnostics (ACD). Cell slides were fixed in cold 4% paraformaldehyde (PFA) for 15 min and then dehydrated through a graded ethanol series (50%, 70%, and 100%), followed by air-drying. After hydrogen peroxide treatment, slides were subjected to protease digestion using RNAscope® H_2O_2 & Protease Plus (ACD, Cat# 322330). For detection of SARS-CoV-2 RNA, a mix of probes targeting the negative strand (RNAscope™ Probe - V-nCoV2019-S, Cat# 848561) and the positive strand (RNAscope™ Probe - V-nCoV2019-orf1ab-sense, Cat# 859151) was applied to the slides for in situ hybridization. Signal amplification and detection were performed using the RNAscope® 2.5 HD Duplex Detection Reagents (ACD, Cat# 322500).

If RNAscope was combined with LC3 immunostaining, slides were blocked in PBS containing 3% fetal calf serum (FCS) for 1 h, followed by overnight incubation with primary antibodies anti-LC3B (1:250 dilution, Nordic Biosite, ARG43536). The following day, slides were incubated with Alexa Fluor-conjugated secondary antibodies (1:500 dilution; Invitrogen) for 1 h. Finally, slides were mounted using DAPI-containing ProLong™ Diamond Antifade Mountant (Thermo Fisher Scientific).

Transmission electron microscopy (TEM)

Wild-Type, FIP200 KO, and FIP200 KI P2 A549-hACE2 cells were cultured in 6-well plates and infected with SARS-COV-2 (Freiburg B.1, MOI 1) for 24 h. Cells were then fixed by adding an equal volume of double-strength fixative (4% paraformaldehyde (PFA), 5% glutaraldehyde in 0.1 M sodium cacodylate buffer, pH 7.4) to the culture medium and incubated for 20 min at room temperature. The fixative mixture was then replaced with 1 ml of single-strength fixative (2% PFA and 2.5% glutaraldehyde in 0.1 M sodium cacodylate buffer, pH 7.4) for another 2 h at room temperature. After 5 washes with 0.1 M sodium cacodylate buffer (pH 7.4), cells were processed for dehydration and embedding in Epon resin[97]. To preserve their original morphology, the monolayer cell cultures were embedded in their original position while in the culture flasks. Subsequently, 70 nm ultrathin sections were cut using a Leica EM UC7 ultra microtome (Leica Microsystems) and stained with uranyl acetate in 70% methanol and lead citrate[97]. Cell sections were analyzed in a 120 kV JEOL JEM 1400 transmission electron microscope (JEOL).

For the statistical analysis, the percentage of cells showing signs of infection, the average number of autophagosomes, of white large vacuole-containing virions (LVCVs), of dark vacuole-containing virions, of degradative compartments (DGCs), and the percentage of DGCs containing virions per cell section was performed by examining 200 cell profiles per condition, randomly selected from four independent grids. A cell was considered infected, i.e., showed a sign of infection, if at least one of the virus-induced structures (DMVs, spherules, and/or virions) was detected in the examined cell section. The structures counted in each infected cell profile were categorized as follows. Autophagosomes were defined as circular structures limited by a double membrane and mainly containing cytoplasmic material. DGCs, which comprise lysosomes, amphisomes, and autolysosomes, were defined as electron-dense structures with heteromorphous content. LVCVs were defined as vacuoles that contained virions in their white lumen. The dark vacuoles were defined as intracellular structures dense to electron (i.e., appearing with a gray or dark gray content) that showed presence of clusters of virions in their lumen. The presence of virions in the degradative compartments was used to calculate the percentage of DGCs containing virions.

Isolation of FLAG-LC3B-positive subcellular vesicles

Wild-type or FIP200-knockout (KO) A549 cells stably expressing the ACE2 receptor were engineered to express FLAG-tagged LC3B. Cells were infected with SARS-CoV-2 at an MOI of 0.1 for 24 h. After infection, cells were harvested and homogenized using a 25-gauge needle (20 passes) in B88 buffer (20 mM HEPES-KOH, pH 7.2, 250 mM sorbitol, 150 mM potassium acetate, 5 mM magnesium acetate), supplemented with protease inhibitor cocktail (Roche) and 0.3 mM dithiotretiol (DTT). Cell lysates were sequentially centrifuged at 1000 × *g* for 10 min and then at 5000 × *g* for an additional 10 min. The resulting supernatants were incubated with 50 µl FLAG-M2 beads for 2 h at 4 °C to enrich FLAG-LC3 positive vesicles. After incubation, beads were washed three times with B88 buffer. FLAG-LC3B vesicles were eluted from the beads using B88 buffer containing FLAG peptide and protease inhibitors. Eluted membranes underwent density gradient fractionation using a modified OptiPrep flotation assay[98,99]. Briefly, a 50% OptiPrep solution was prepared in B88 buffer and combined with eluted vesicles to obtain a final 40% OptiPrep solution in a total volume of 1 ml. This solution was carefully overlayed with 1 ml of 35% OptiPrep

and topped with 50 µl of B88 buffer. Gradients were centrifuged at 150,000 × *g* for 3 h at 4 °C. Twelve fractions of 150 µl each were collected from the gradient bottom to top. For Western blot analysis, fractions were precipitated using methanol–chloroform extraction prior to immunoblotting. For qPCR, fractions 6–12 from the top were further centrifuged at 100,000 × *g* for 1 h to pellet vesicles. RNA was extracted from pelleted vesicles and subjected to qPCR analysis.

General statistical analyses

Experiments were performed in biological triplicates. Statistical analyses were carried out using GraphPad Prism (version 8). Depending on data distribution, either parametric or nonparametric tests were applied. Brown–Forsythe and Welch ANOVA tests with two-sided Dunnett's T3 multiple comparison correction, one-way ANOVA with two-sided Dunnett's or Tukey's multiple comparison correction, or Kruskal–Wallis tests with two-sided Dunn's correction were used as appropriate. Pairwise comparisons were analyzed using two-sided Student's t-tests with Bonferroni correction, unpaired Welch's *t*-tests with the two-stage linear step-up procedure, or two-sided Mann–Whitney tests with Bonferroni correction. All tests were two-sided, and p-values <0.05 were considered statistically significant.

Ethics

The patients and healthy controls were included following oral and written consent and in accordance with The Helsinki Declaration and national ethics guidelines after approval from the Danish National Committee on Health Ethics (1-10-72-80-20), the Data Protection Agency, and the Institutional Review Board.

Air–liquid interface pulmonary epithelium cells were collected and cultured as approved by The Science Ethical Committee (Den Videnskabsetiske Komitéer) for the Region of Midtjylland with case number 1-10-72-182-19.

The Danish Animal Experiments Inspectorate has approved the experimental animal procedures, which were carried out in accordance with the Danish Animal Welfare Act for the Care and Use of Animals for Scientific Purposes (License ID 2019-15-0201-00090 and 2020-15-0201-00726). All procedures followed the recommendations of the Animal Facilities at the Universities of Copenhagen and Aarhus.

Reporting summary

Further information on research design is available in the Nature Portfolio Reporting Summary linked to this article.

Data availability

Additional information on the clinical history of the two patients and the entire cohort is available in the Supplementary Material. Further information on the genetic analysis, sequencing data, or methodologies can be requested from the authors and will be shared with healthcare professionals and scientists in accordance with national and international rules and regulations for patient ethics, data sharing, and data protection. Source data are provided with this paper.

References

1. Lu, R. et al. Genomic characterisation and epidemiology of 2019 novel coronavirus: implications for virus origins and receptor binding. *Lancet* **395**, 565–574 (2020).
2. Chan, J. F. et al. A familial cluster of pneumonia associated with the 2019 novel coronavirus indicating person-to-person transmission: a study of a family cluster. *Lancet* **395**, 514–523 (2020).
3. Del Sole, F. et al. Features of severe COVID-19: a systematic review and meta-analysis. *Eur. J. Clin. Investig.* **50**, e13378 (2020).
4. O'Driscoll, M. et al. Age-specific mortality and immunity patterns of SARS-CoV-2. *Nature* **590**, 140–145 (2021).
5. Jackson, C. B., Farzan, M., Chen, B. & Choe, H. Mechanisms of SARS-CoV-2 entry into cells. *Nat. Rev. Mol. Cell Biol.* **23**, 3–20 (2022).
6. Hoffmann, M. et al. SARS-CoV-2 cell entry depends on ACE2 and TMPRSS2 and is blocked by a clinically proven protease inhibitor. *Cell* **181**, 271–280.e278 (2020).
7. Han, B. et al. ACE2-independent SARS-CoV-2 virus entry through cell surface GRP78 on monocytes—evidence from a translational clinical and experimental approach. *EBioMedicine* **98**, 104869 (2023).
8. Paludan, S. R. & Mogensen, T. H. Innate immunological pathways in COVID-19 pathogenesis. *Sci. Immunol.* **7**, eabm5505 (2022).
9. Mantovani, S., Oliviero, B., Varchetta, S., Renieri, A. & Mondelli, M. U. TLRs: innate immune sentries against SARS-CoV-2 infection. *Int J. Mol. Sci.* **24**, 8065 (2023).
10. Bortolotti, D. et al. TLR3 and TLR7 RNA sensor activation during SARS-CoV-2 infection. *Microorganisms* **9**, 1820 (2021).
11. van der Sluis, R. M. et al. TLR2 and TLR7 mediate distinct immunopathological and antiviral plasmacytoid dendritic cell responses to SARS-CoV-2 infection. *EMBO J.* **41**, e109622 (2022).
12. Sampaio, N. G. et al. The RNA sensor MDA5 detects SARS-CoV-2 infection. *Sci. Rep.* **11**, 13638 (2021).
13. Diamond, M. S. & Kanneganti, T. D. Innate immunity: the first line of defense against SARS-CoV-2. *Nat. Immunol.* **23**, 165–176 (2022).
14. Minkoff, J. M. & tenOever, B. Innate immune evasion strategies of SARS-CoV-2. *Nat. Rev. Microbiol.* **21**, 178–194 (2023).
15. COVID-19 Forecasting Team Variation in the COVID-19 infection-fatality ratio by age, time, and geography during the pre-vaccine era: a systematic analysis. *Lancet* **399**, 1469–1488 (2022).
16. Zhang, Q. et al. Inborn errors of type I IFN immunity in patients with life-threatening COVID-19. *Science* **370**, eabd4570 (2020).
17. Zhang, Q., Bastard, P., Effort, C. H. G., Cobat, A. & Casanova, J. L. Human genetic and immunological determinants of critical COVID-19 pneumonia. *Nature* **603**, 587–598 (2022).
18. Bastard, P. et al. Autoantibodies neutralizing type I IFNs are present in ~4% of uninfected individuals over 70 years old and account for ~20% of COVID-19 deaths. *Sci. Immunol.* **6**, eabl4340 (2021).
19. Bastard, P. et al. Autoantibodies against type I IFNs in patients with life-threatening COVID-19. *Science* **370**, eabd4585 (2020).
20. Orvedahl, A. et al. Autophagy protects against Sindbis virus infection of the central nervous system. *Cell Host Microbe* **7**, 115–127 (2010).
21. Tian, Y., Wang, M. L. & Zhao, J. Crosstalk between autophagy and type I interferon responses in innate antiviral immunity. *Viruses* **11**, 132 (2019).
22. Boya, P., Reggiori, F. & Codogno, P. Emerging regulation and functions of autophagy. *Nat. Cell Biol.* **15**, 713–720 (2013).
23. Pradel, B., Robert-Hebmann, V. & Espert, L. Regulation of innate immune responses by autophagy: a goldmine for viruses. *Front. Immunol.* **11**, 578038 (2020).
24. Thyrsted, J. et al. Influenza A induces lactate formation to inhibit type I IFN in primary human airway epithelium. *iScience* **24**, 103300 (2021).
25. Levine, B. & Kroemer, G. Biological functions of autophagy genes: a disease perspective. *Cell* **176**, 11–42 (2019).
26. Miller, K. et al. Coronavirus interactions with the cellular autophagy machinery. *Autophagy* **16**, 2131–2139 (2020).
27. Lamark, T. & Johansen, T. Mechanisms of selective autophagy. *Annu. Rev. Cell Dev. Biol.* **37**, 143–169 (2021).
28. Galluzzi, L. & Green, D. R. Autophagy-independent functions of the autophagy machinery. *Cell* **177**, 1682–1699 (2019).
29. Sanjuan, M. A. et al. Toll-like receptor signalling in macrophages links the autophagy pathway to phagocytosis. *Nature* **450**, 1253–1257 (2007).
30. Lystad, A. H. & Simonsen, A. Mechanisms and pathophysiological roles of the ATG8 conjugation machinery. *Cells* **8**, 973 (2019).
31. Kaushik, S. & Cuervo, A. M. The coming of age of chaperone-mediated autophagy. *Nat. Rev. Mol. Cell Biol.* **19**, 365–381 (2018).

32. Schuck, S. Microautophagy—distinct molecular mechanisms handle cargoes of many sizes. *J. Cell Sci.* **133**, jcs246322 (2020).
33. De Duve, C. & Wattiaux, R. Functions of lysosomes. *Annu. Rev. Physiol.* **28**, 435–492 (1966).
34. Deretic, V. Autophagy in inflammation, infection, and immunometabolism. *Immunity* **54**, 437–453 (2021).
35. Ahmad, L., Mostowy, S. & Sancho-Shimizu, V. Autophagy-virus interplay: from cell biology to human disease. *Front. Cell Dev. Biol.* **6**, 155 (2018).
36. He, W. et al. Friend or foe? Implication of the autophagy-lysosome pathway in SARS-CoV-2 infection and COVID-19. *Int. J. Biol. Sci.* **18**, 4690–4703 (2022).
37. Mauthe, M. & Reggiori, F. ATG proteins: Are we always looking at autophagy?. *Autophagy* **12**, 2502–2503 (2016).
38. Alirezaei, M., Flynn, C. T., Wood, M. R., Harkins, S. & Whitton, J. L. Coxsackievirus can exploit LC3 in both autophagy-dependent and -independent manners in vivo. *Autophagy* **11**, 1389–1407 (2015).
39. Mauthe, M. et al. An siRNA screen for ATG protein depletion reveals the extent of the unconventional functions of the autophagy proteome in virus replication. *J. Cell Biol.* **214**, 619–635 (2016).
40. Reggiori, F. et al. Coronaviruses Hijack the LC3-I-positive EDEMosomes, ER-derived vesicles exporting short-lived ERAD regulators, for replication. *Cell Host Microbe* **7**, 500–508 (2010).
41. Sabli, I. K. & Sancho-Shimizu, V. Inborn errors of autophagy and infectious diseases. *Curr. Opin. Immunol.* **72**, 272–276 (2021).
42. Hait, A. S. et al. Defects in LC3B2 and ATG4A underlie HSV2 meningitis and reveal a critical role for autophagy in antiviral defense in humans. *Sci. Immunol.* **5**, eabc2691 (2020).
43. Brinck Andersen, N. S. et al. Essential role of autophagy in restricting poliovirus infection revealed by identification of an ATG7 defect in a poliomyelitis patient. *Autophagy* **17**, 2449–2464 (2021).
44. Acharya, D. et al. TRIM23 mediates cGAS-induced autophagy in anti-HSV defense. *Nat. Commun.* **16**, 4418 (2025).
45. Bousfiha, A. et al. The 2022 update of IUIS phenotypical classification for human inborn errors of immunity. *J. Clin. Immunol.* **42**, 1508–1520 (2022).
46. Matuozzo, D. et al. Rare predicted loss-of-function variants of type I IFN immunity genes are associated with life-threatening COVID-19. *Genome Med.* **15**, 22 (2023).
47. Hertrich, I. & Ziegelmayer, G. [The voice as an anthropologic marker system, its constitutional correlates and characteristics]. *Anthropol. Anz.* **46**, 185–193 (1988).
48. Rapaport, F. et al. Negative selection on human genes underlying inborn errors depends on disease outcome and both the mode and mechanism of inheritance. *Proc. Natl. Acad. Sci. USA* **118**, e2001248118 (2021).
49. Jalloh, S. et al. CD169-mediated restrictive SARS-CoV-2 infection of macrophages induces pro-inflammatory responses. *PLoS Pathog.* **18**, e1010479 (2022).
50. Garcia-Nicolas, O., Godel, A., Zimmer, G. & Summerfield, A. Macrophage phagocytosis of SARS-CoV-2-infected cells mediates potent plasmacytoid dendritic cell activation. *Cell. Mol. Immunol.* **20**, 835–849 (2023).
51. Kazmierski, J. et al. Nonproductive exposure of PBMCs to SARS-CoV-2 induces cell-intrinsic innate immune responses. *Mol. Syst. Biol.* **18**, e10961 (2022).
52. Essa, S. et al. Influence of SARS-COV-2 infection on cytokine production by mitogen-stimulated peripheral blood mononuclear cells and neutrophils in COVID-19 intensive care unit patients. *Microorganisms* **10**, 2194 (2022).
53. Chen, X. et al. International consensus guidelines for the definition, detection, and interpretation of autophagy-dependent ferroptosis. *Autophagy* **20**, 1213–1246 (2024).
54. Schoggins, J. W. et al. A diverse range of gene products are effectors of the type I interferon antiviral response. *Nature* **472**, 481–485 (2011).
55. Ulasli, M., Verheije, M. H., de Haan, C. A. & Reggiori, F. Qualitative and quantitative ultrastructural analysis of the membrane rearrangements induced by coronavirus. *Cell. Microbiol.* **12**, 844–861 (2010).
56. Deretic, V. et al. Membrane atg8ylation in canonical and non-canonical autophagy. *J. Mol. Biol.* **436**, 168532 (2024).
57. Yuan, Z. et al. ATG14 targets lipid droplets and acts as an autophagic receptor for syntaxin18-regulated lipid droplet turnover. *Nat. Commun.* **15**, 631 (2024).
58. Kumar, S., Jia, J. & Deretic, V. Atg8ylation as a general membrane stress and remodeling response. *Cell Stress* **5**, 128–142 (2021).
59. Kirkin, V. & Rogov, V. V. A diversity of selective autophagy receptors determines the specificity of the autophagy pathway. *Mol. Cell* **76**, 268–285 (2019).
60. Rogov, V. V. et al. Atg8 family proteins, LIR/AIM motifs and other interaction modes. *Autophagy Rep.* **2**, 2188523 (2023).
61. Khaminets, A. et al. Regulation of endoplasmic reticulum turnover by selective autophagy. *Nature* **522**, 354–358 (2015).
62. Chiramel, A. I., Dougherty, J. D., Nair, V., Robertson, S. J. & Best, S. M. FAM134B, the selective autophagy receptor for endoplasmic reticulum turnover, inhibits replication of ebola virus strains Makona and Mayinga. *J. Infect. Dis.* **214**, S319–S325 (2016).
63. Zhang, X. et al. SARS-CoV-2 ORF3a induces RETREG1/FAM134B-dependent reticulophagy and triggers sequential ER stress and inflammatory responses during SARS-CoV-2 infection. *Autophagy* **18**, 2576–2592 (2022).
64. Tan, X. et al. Coronavirus subverts ER-phagy by hijacking FAM134B and ATL3 into p62 condensates to facilitate viral replication. *Cell Rep.* **42**, 112286 (2023).
65. Verlhac, P. et al. Autophagy receptor NDP52 regulates pathogen-containing autophagosome maturation. *Cell Host Microbe* **17**, 515–525 (2015).
66. Shi, X., Chang, C., Yokom, A. L., Jensen, L. E. & Hurley, J. H. The autophagy adaptor NDP52 and the FIP200 coiled-coil allosterically activate ULK1 complex membrane recruitment. *eLife* **9**, e59099 (2020).
67. Paludan, S. R. et al. Early host defense against virus infections. *Cell Rep.* **43**, 115070 (2024).
68. Yeo, S. K., Wang, C. & Guan, J. L. Role of FIP200 in inflammatory processes beyond its canonical autophagy function. *Biochem. Soc. Trans.* **48**, 1599–1607 (2020).
69. Shi, X. et al. ULK complex organization in autophagy by a C-shaped FIP200 N-terminal domain dimer. *J. Cell Biol.* **219**, e201911047 (2020).
70. Watson, R. O. et al. The cytosolic sensor cGAS detects Mycobacterium tuberculosis DNA to induce type i interferons and activate autophagy. *Cell Host Microbe* **17**, 811–819 (2015).
71. Schmidt, K. W. et al. Selective autophagy impedes KSHV entry after recruiting the membrane damage sensor galectin-8 to virus-containing endosomes. *Cell Rep.* **43**, 115019 (2024).
72. Yakoub, A. M. & Shukla, D. Autophagy stimulation abrogates herpes simplex virus-1 infection. *Sci. Rep.* **5**, 9730 (2015).
73. Hafren, A. et al. Selective autophagy limits cauliflower mosaic virus infection by NBR1-mediated targeting of viral capsid protein and particles. *Proc. Natl. Acad. Sci. USA* **114**, E2026–E2035 (2017).
74. Paludan, S. R., Pradeu, T., Masters, S. L. & Mogensen, T. H. Constitutive immune mechanisms: mediators of host defence and immune regulation. *Nat. Rev. Immunol.* **21**, 137–150 (2021).
75. Viret, C., Duclaux-Loras, R., Nancey, S., Rozieres, A. & Faure, M. Selective autophagy receptors in antiviral defense. *Trends Microbiol.* **29**, 798–810 (2021).

76. Liu, Y. et al. Targeting selective autophagy as a therapeutic strategy for viral infectious diseases. *Front. Microbiol.* **13**, 889835 (2022).
77. Wen, W. et al. Selective autophagy receptor SQSTM1/ p62 inhibits Seneca Valley virus replication by targeting viral VP1 and VP3. *Autophagy* **17**, 3763–3775 (2021).
78. Rogov, V., Dotsch, V., Johansen, T. & Kirkin, V. Interactions between autophagy receptors and ubiquitin-like proteins form the molecular basis for selective autophagy. *Mol. Cell* **53**, 167–178 (2014).
79. Fan, S. et al. The role of autophagy and autophagy receptor NDP52 in microbial infections. *Int. J. Mol. Sci.* **21**, 2008 (2020).
80. Jin, S. et al. Tetherin suppresses type I interferon signaling by targeting MAVS for NDP52-mediated selective autophagic degradation in human cells. *Mol. Cell* **68**, 308–322.e304 (2017).
81. Goodwin, J. M. et al. Autophagy-independent lysosomal targeting regulated by ULK1/2-FIP200 and ATG9. *Cell Rep.* **20**, 2341–2356 (2017).
82. Wang, L. et al. FIP200 restricts RNA virus infection by facilitating RIG-I activation. *Commun. Biol.* **4**, 921 (2021).
83. Tal, M. C. et al. Absence of autophagy results in reactive oxygen species-dependent amplification of RLR signaling. *Proc. Natl. Acad. Sci. USA* **106**, 2770–2775 (2009).
84. Prabakaran, T. et al. Attenuation of cGAS-STING signaling is mediated by a p62/SQSTM1-dependent autophagy pathway activated by TBK1. *EMBO J.* **37**, e97858 (2018).
85. Shi, C. S. et al. Activation of autophagy by inflammatory signals limits IL-1beta production by targeting ubiquitinated inflammasomes for destruction. *Nat. Immunol.* **13**, 255–263 (2012).
86. Gassen, N. C. et al. SARS-CoV-2-mediated dysregulation of metabolism and autophagy uncovers host-targeting antivirals. *Nat. Commun.* **12**, 3818 (2021).
87. Resnik, R. et al. Autophagy in inflammatory response against SARS-CoV-2. *Int. J. Mol. Sci.* **24**, 4928 (2023).
88. Wei, H. et al. Suppression of autophagy by FIP200 deletion inhibits mammary tumorigenesis. *Genes Dev.* **25**, 1510–1527 (2011).
89. Chen, S. et al. Distinct roles of autophagy-dependent and -independent functions of FIP200 revealed by generation and analysis of a mutant knock-in mouse model. *Genes Dev.* **30**, 856–869 (2016).
90. Nissen, S. K. et al. Whole Exome Sequencing of HIV-1 long-term non-progressors identifies rare variants in genes encoding innate immune sensors and signaling molecules. *Sci. Rep.* **8**, 15253 (2018).
91. Jorgensen, S. E. et al. Defective RNA sensing by RIG-I in severe influenza virus infection. *Clin. Exp. Immunol.* **192**, 366–376 (2018).
92. Reed, L. J. & Muench, H. A simple method of estimating fifty per cent endpoints. *Am. J. Epidemiol.* **27**, 493–497 (1938).
93. Marino, G. et al. STING is redundant for host defense and pathology of COVID-19-like disease in mice. *Life Sci. Alliance* **6**, e202301997 (2023).
94. Laustsen, A. et al. Interferon priming is essential for human CD34+ cell-derived plasmacytoid dendritic cell maturation and function. *Nat. Commun.* **9**, 3525 (2018).
95. Hardie, D. C., Gregory, T. R. & Hebert, P. D. From pixels to picograms: a beginners' guide to genome quantification by Feulgen image analysis densitometry. *J. Histochem. Cytochem.* **50**, 735–749 (2002).
96. de Chaumont, F. et al. Icy: an open bioimage informatics platform for extended reproducible research. *Nat. Methods* **9**, 690–696 (2012).
97. Verheije, M. H. et al. Mouse hepatitis coronavirus RNA replication depends on GBF1-mediated ARF1 activation. *PLoS Pathog.* **4**, e1000088 (2008).
98. Ge, L., Melville, D., Zhang, M. & Schekman, R. The ER-Golgi intermediate compartment is a key membrane source for the LC3 lipidation step of autophagosome biogenesis. *eLife* **2**, e00947 (2013).
99. Zhang, B. C. et al. STEEP mediates STING ER exit and activation of signaling. *Nat. Immunol.* **21**, 868–879 (2020).

Acknowledgements

The authors wish to thank the patients for participating in the study. In addition, the authors are thankful to Bettina Bundgaard for skillful technical assistance and to the COVID Human Genetic effort for discussions, collaboration, and data sharing. For funding, T.H.M. has received funding from The Independent Research Council (0134-00006B) and the Novo Nordisk Foundation (NNF21OC0067157 and NNF20OC0064890) and Horizon Europe 2021, HORIZON-HLTH-2021-DISEASE-04-07 (UNDINE 101057100). S.R.P. and T.H.M. are supported by the Danish National Research Foundation (DNRF164). F.R. is supported by Novo Nordisk Foundation (0066384) and Lundbeck Foundation (R383-2022-180) grants. The Laboratory of Human Genetics of Infectious Diseases is supported by the Howard Hughes Medical Institute, The Rockefeller University, the St. Giles Foundation, the Stavros Niarchos Foundation (SNF) as part of its grant to the SNF Institute for Global Infectious Disease Research at The Rockefeller University, the National Institutes of Health (NIH) (R01AI163029, R01AI088364), the National Center for Advancing Translational Sciences (NCATS), the NIH Clinical and Translational Science Award (CTSA) program (UL1TR001866), the Fisher Center for Alzheimer's Research Foundation, the Meyer Foundation, the JPB Foundation, the French National Research Agency (ANR) under the "Investments for the Future" program (ANR-10-IAHU-01), the Integrative Biology of Emerging Infectious Diseases Laboratory of Excellence (ANR-10-LABX-62-IBEID), the French Foundation for Medical Research (FRM) (EQU201903007798), ANR GENVIR (ANR-20-CE93-003), ANR AI2D (ANR-22-CE15-278 0046), ANR GENFLU (ANR-22-CE92-0004), ANR CNSVIRGEN (ANR-19-CE15-0009-01), the HORIZON-HLTH-2021-DISEASE-04 program under grant agreement 101057100 (UNDINE), the ANR-RHU COVIFERON Program (ANR-21-RHUS-08), the Square Foundation, Grandir - Fonds de solidarité pour l'enfance, the Fondation du Souffle, the SCOR Corporate Foundation for Science, the Battersea & Bowery Advisory Group, William E. Ford, General Atlantic's Chairman and Chief Executive Officer, Gabriel Caillaux, General Atlantic's Co-President, Managing Director and Head of Business in EMEA, and the General Atlantic Foundation, the French Ministry of Higher Education, Research, and Innovation (MESRI-COVID-19), Institut National de la Santé et de la Recherche Médicale (INSERM), REACTing-INSERM, Paris Cité University, and the Imagine Institute. A.G. was supported by a French governmental grant from the French National Agency for Research as part of the Investissement d'Avenir program (ANR-10-LABX-62-01). P.B. was supported by the MD-PhD program of the Imagine Institute (with support from the Bettencourt-Schueller Foundation), a "Poste CCA-INSERM-Bettencourt" (with support from the Bettencourt-Schueller Foundation), and the FRM (EA20170638020).

Author contributions

T.H.M. conceived the idea, identified patients, and planned the project together with S.R.P., F.R., and J.L.C. A.R. cared for patients and collected patient consent and material; L.H., R.v.d.S., and S.E.J. performed WES analysis, assisted by A.C. for population genetics. L.H., R.v.d.S., B.C.Z., T.Z., M.W., A.P., A.L.H., R.N., L.S.R., and B.B. generated data, and L.H., R.v.d.S., B.C.Z., and T.Z. analyzed data together with C.K.H., A.R., J.L.C., S.R.P., and T.H.M. K.B.C. and L.H. performed experiments for EM and analyzed data together with M.M. and F.R. T.H.M. wrote the first draft of the manuscript with input from L.H., R.v.d.S., S.R.P., F.R., and J.L.C. All authors read and approved the final version of the manuscript and participated in the revision process and preparation of the final manuscript and figures. Danish COVID Clinicians were part of the group collecting and handling patient material, and UNDINE and COVID Human Genetic Effort contributed with comparative genome sequencing data, discussions, and study design.

Competing interests
The authors declare no competing interests.

Additional information
Supplementary information The online version contains supplementary material available at https://doi.org/10.1038/s41467-025-65308-8.

Correspondence and requests for materials should be addressed to Trine H. Mogensen.

Peer review information *Nature Communications* thanks Sumana Sanyal and the other, anonymous, reviewer(s) for their contribution to the peer review of this work. A peer review file is available.

COVID Human Genetic Effort

Laurent Abel[4,5,6], Alessandro Aiuti[10,11], Saleh Al-Muhsen[12], Fahd Al-Mulla[13], Mark S. Anderson[14], Evangelos Andreakos[15], Andrés A. Arias[6,16,17], Lisa M. Arkin[18], Hagit Baris Feldman[19], Paul Bastard[4,5,6], Alexandre Belot[20], Catherine M. Biggs[21], Dusan Bogunovic[22], Alexandre Bolze[23], Anastasiia Bondarenko[24], Alessandro Borghesi[25,26], Ahmed A. Bousfiha[27,28], Petter Brodin[29], Yenan Bryceson[30], Jean-Laurent Casanova[4,5,6,7,8], Giorgio Casari[11,31], John Christodoulou[32], Aurélie Cobat[4,5,6], Roger Colobran[33], Antonio Condino-Neto[34], Stefan N. Constantinescu[35], Megan A. Cooper[36], Clifton L. Dalgard[37], Murkesh Desai[38], Beth A. Drolet[39], Munis Dündar[40], Xavier Duval[41,42], Sotirija Duvlis[43,44], Jamila El Baghdadi[45], Philippine Eloy[46], Sara Espinosa-Padilla[47], Jacques Fellay[48,49], Carlos Flores[50,51,52,53], José Luis Franco[16], Antoine Froidure[54,55], Guy Gorochov[56], Marta Gut[57], Filomeen Haerynck[58], David Hagin[59], Rabih Halwani[60], Lennart Hammarström[61], James R. Heath[62], Elena W. Y. Hsieh[63], Eystein Husebye[64], Kohsuke Imai[65], Yuval Itan[66,67], Emmanuelle Jouanguy[4,5,6], Elżbieta Kaja[68], Timokratis Karamitros[69], Kai Kisand[70], Cheng-Lung Ku[71], Yu-Lung Lau[72], Yun Ling[73], Carrie L. Lucas[74], Matthieu Mahévas[75,76], Davood Mansouri[77], László Maródi[78], France Mentré[41,79], Isabelle Meyts[80,81], Joshua D. Milner[82], Kristina Mironska[83], Trine H. Mogensen[1,2,9] ✉, Tomohiro Morio[84], Lisa F. P. Ng[85,86], Luigi D. Notarangelo[87], Antonio Novelli[88], Giuseppe Novelli[89], Cliona O'Farrelly[90], Satoshi Okada[91], Keisuke Okamoto[92], Tayfun Ozcelik[93], Firat Ozcelik[94], Qiang Pan-Hammarström[61], Rebeca Perez de Diego[95,96], Jordi Perez-Tur[97,98], David S. Perlin[99], Jonny Peter[100,101], Anna M. Planas[102], Carolina Prando[103], Aurora Pujol[104,105,106], Anne Puel[4,5,6], Lluis Quintana-Murci[107,108], Sathishkumar Ramaswamy[109], Laurent Renia[85,86], Igor Resnick[110], Carlos Rodríguez-Gallego[111,112,113,114], Vanessa Sancho-Shimizu[115,116], Anna Sediva[117], Mikko R. J. Seppänen[118,119], Mohammad Shahrooei[120], Anna Shcherbina[121], Ondrej Slaby[122], Andrew L. Snow[123], Pere Soler-Palacín[124], Vassili Soumelis[125,126], András N. Spaan[127], Helen C. Su[87], Ivan Tancevski[128], Stuart G. Tangye[129,130], Ahmad Abou Tayoun[109], Şehime Gülsün Temel[131], Christian Thorball[49], Pierre Tiberghien[132], Sophie Trouillet-Assant[133,134], Stuart E. Turvey[135], K. M. Furkan Uddin[136], Mohammed J. Uddin[137,138], Diederik van de Beek[139], Fernanda Sales Luiz Vianna[140,141], Donald C. Vinh[142,143], Horst von Bernuth[144,145,146], Joost Wauters[147], Mayana Zatz[148], Qian Zhang[4,5,6], Shen-Ying Zhang[4,5,6], Jacob Bodilsen[149], Kristoffer Skaalum Hansen[9], Merete Storgaard[149], Thomas Benfield[150] & Marie Helleberg[151]

[10]Pediatric Immunohematology and Bone Marrow Transplantation Unit & San Raffaele Telethon Institute for Gene Therapy, IRCCS San Raffaele Scientific Institute, Milan, Italy. [11]Vita-Salute San Raffaele University, Milan, Italy. [12]Immunology Research Lab, Department of Pediatrics, College of Medicine, King Saud University, Riyadh, Saudi Arabia. [13]Dasman Diabetes Institute, Department of Genetics and Bioinformatics, Kuwait City, Kuwait. [14]Diabetes Center, University of California San Francisco, San Francisco, CA, USA. [15]Laboratory of Immunobiology, Center for Clinical, Experimental Surgery and Translational Research, Biomedical Research Foundation of the Academy of Athens, Athens, Greece. [16]Inborn Errors of Immunity Group, (Primary Immunodeficiencies), School of Medicine, University of Antioquia UdeA, Medellín, Colombia. [17]School of Microbiology, University of Antioquia UdeA, Medellín, Colombia. [18]Department of Dermatology, School of Medicine and Public Health, University of Wisconsin-Madison, Madison, WI, USA. [19]Genetics Institute and Genomics Center, Tel Aviv Sourasky Medical Center and Faculty of Medical & Health Sciences, Tel Aviv University, Tel Aviv, Israel. [20]Pediatric Nephrology, Rheumatology, Dermatology, HFME, Hospices Civils de Lyon, National Referee Centre RAISE, and INSERM U1111, Université de Lyon, Lyon, France. [21]Department of Pediatrics, BC Children's and St. Paul's Hospitals, University of British Columbia, Vancouver, BC, Canada. [22]Department of Pediatrics, Center for Genetic Errors of Immunity, Columbia

University, New York, NY, USA. [23]Helix, San Mateo, CA, USA. [24]International European University, Kyiv, Ukraine. [25]San Matteo Research Hospital, Pavia, Italy. [26]Geneva University Hospitals (HUG) & University of Geneva, Geneva, Switzerland. [27]Clinical Immunology and Infectious Pediatrics Department, Abderrahim Harouchi Hospital-Ibn Rochd University Hospital, Casablanca, Morocco. [28]Laboratory of Clinical Immunology-Inflammation and Allergy (LICIA), Faculty of Medicine and Pharmacy, Hassan II University, Casablanca, Morocco. [29]SciLifeLab, Department of Women's and Children's Health, Karolinska Institutet, Stockholm, Sweden. [30]Department of Medicine, Center for Hematology and Regenerative Medicine, Karolinska Institutet, Stockholm, Sweden. [31]Genomic Unit for the Diagnosis of Human Pathologies, IRCCS San Raffaele Scientific Institute, Milan, Italy. [32]Murdoch Children's Research Institute and Department of Paediatrics, University of Melbourne, Melbourne, VIC, Australia. [33]Immunology Division, Genetics Department, Hospital Universitari Vall d'Hebron, Vall d'Hebron Research Institute, Vall d'Hebron Barcelona Hospital Campus, UAB, Barcelona, Spain. [34]Department of Immunology, Institute of Biomedical Sciences, University of São Paulo, São Paulo, Brazil. [35]de Duve Institute, UC Louvain and Ludwig Cancer Research, Brussels, Belgium. [36]Washington University School of Medicine, St. Louis, MO, USA. [37]Department of Anatomy, Physiology & Genetics, Uniformed Services University of the Health Sciences, Bethesda, MD, USA. [38]Bai Jerbai Wadia Hospital for Children, Mumbai, India. [39]School of Medicine and Public Health, University of Wisconsin, Madison, WI, USA. [40]Department of Medical Genetics, Faculty of Medicine, Erciyes University, Kayseri, Turkey. [41]Paris Cité University, IAME, INSERM, Paris, France. [42]AP-HP, Centre d'Investigation Clinique, INSERM CIC 1425, Hôpital Bichat, Paris, France. [43]Faculty of Medical Sciences, University "Goce Delchev", Stip, Shtip, North Macedonia. [44]Institute of Public Health of the Republic of North Macedonia, Skopje, North Macedonia. [45]Genetics Unit, Military Hospital Mohamed V, Rabat, Morocco. [46]Hôpital Bichat, Paris, France. [47]Immune Deficiencies Laboratory, National Institute of Pediatrics, Mexico City, Mexico. [48]School of Life Sciences, Ecole Polytechnique Fédérale de Lausanne, Lausanne, Switzerland. [49]Precision Medicine Unit, Lausanne University Hospital and University of Lausanne, Lausanne, Switzerland. [50]Research Unit, Hospital Universitario Nuestra Señora de Candelaria, Santa Cruz de Tenerife, Spain. [51]Genomics Division, Instituto Tecnológico y de Energías Renovables (ITER), Santa Cruz de Tenerife, Spain. [52]Faculty of Health Sciences, University of Fernando Pessoa Canarias, Las Palmas de Gran Canaria, Spain. [53]CIBER de Enfermedades Respiratorias, Instituto de Salud Carlos III, Madrid, Spain. [54]Pulmonology Department, Cliniques Universitaires Saint-Luc, Sierre, Switzerland. [55]Institut de Recherche Expérimentale et Clinique (IREC), Université Catholique de Louvain, Brussels, Belgium. [56]Sorbonne Université, Inserm, Centre d'Immunologie et des Maladies Infectieuses-Paris (CIMI PARIS), Assistance Publique-Hôpitaux de Paris (AP-HP), Hôpital Pitié-Salpêtrière, Paris, France. [57]Centro Nacional de Análisis Genómico (CNAG), University of Barcelona, Barcelona, Spain. [58]Department of Paediatric Immunology and Pulmonology, Centre for Primary Immunodeficiency Ghent (CPIG), PID Research Laboratory, Jeffrey Modell Diagnosis and Research Centre, Ghent University Hospital, Ghent, Belgium. [59]Allergy and Clinical Immunology Unit, Department of Medicine, Tel Aviv Sourasky Medical Center and Tel Aviv University, Tel Aviv, Israel. [60]Research Institute for Medical and Health Sciences, University of Sharjah, Sharjah, United Arab Emirates. [61]Department of Medical Biochemistry and Biophysics, Karolinska Institutet, Stockholm, Sweden. [62]Institute for Systems Biology, Seattle, WA, USA. [63]Departments of Pediatrics, Immunology and Microbiology, School of Medicine, University of Colorado, Aurora, CO, USA. [64]Department of Medicine, Haukeland University Hospital, Bergen, Norway. [65]National Defense Medical College (NDMC), Saitama, Japan. [66]Institute for Personalized Medicine, Icahn School of Medicine at Mount Sinai, New York, NY, USA. [67]Department of Genetics and Genomic Sciences, Icahn School of Medicine at Mount Sinai, New York, NY, USA. [68]Department of Medical Chemistry and Laboratory Medicine, Poznan University of Medical Sciences, Poznan, Poland. [69]Bioinformatics and Applied Genomics Unit, Hellenic Pasteur Institute, Athens, Greece. [70]Molecular Pathology, Department of Biomedicine, Institute of Biomedicine and Translational Medicine, University of Tartu, Tartu, Estonia. [71]Chang Gung University, Taoyuan City, Taiwan, ROC. [72]Department of Paediatrics & Adolescent Medicine, The University of Hong Kong, Hong Kong, China. [73]Shanghai Public Health Clinical Center, Fudan University, Shanghai, China. [74]Department of Immunobiology, Yale University School of Medicine, New Haven, CT, USA. [75]Necker Enfants Malades Institute (INEM), INSERM U1151/CNRS UMR 8253, University of Paris Cité, Paris, France. [76]Department of Internal Medicine, Henri Mondor University Hospital, Assistance Publique-Hôpitaux de Paris (AP-HP), Paris-Est Créteil University (UPEC), Paris, France. [77]Department of Clinical Immunology and Infectious Diseases, National Research Institute of Tuberculosis and Lung Diseases, The Clinical Tuberculosis and Epidemiology Research Center, National Research Institute of Tuberculosis and Lung Diseases (NRITLD), Masih Daneshvari Hospital, Shahid Beheshti, University of Medical Sciences, Tehran, Iran. [78]Primary Immunodeficiency Clinical Unit and Laboratory, Department of Dermatology, Venereology and Dermatooncology, Semmelweis University, Budapest, Hungary. [79]AP-HP, Department of Epidemiology, Biostatistics and Clinical Research, Hôpital Bichat, Paris, France. [80]Department of Pediatrics, University Hospitals Leuven, Leuven, Belgium. [81]Laboratory for Inborn Errors of Immunity, Department of Microbiology, Immunology and Transplantation, KU Leuven, Leuven, Belgium. [82]Department of Pediatrics, Columbia University Irving Medical Center, New York, NY, USA. [83]University Clinic for Children's Diseases, Department of Pediatric Immunology, Medical Faculty, University "St.Cyril and Methodij", Skopje, North Macedonia. [84]Tokyo Medical & Dental University Hospital, Tokyo, Japan. [85]A*STAR Infectious Diseases Labs (A*STAR IDL), Agency for Science, Technology and Research, Singapore, Singapore. [86]Lee Kong Chian School of Medicine, Nanyang Technological University, Nanyang, Singapore. [87]National Institute of Allergy and Infectious Diseases, National Institutes of Health, Bethesda, MD, USA. [88]Laboratory of Medical Genetics, IRCCS Bambino Gesù Children's Hospital, Rome, Italy. [89]Department of Biomedicine and Prevention, Tor Vergata University of Rome, Rome, Italy. [90]Comparative Immunology Group, School of Biochemistry and Immunology, Trinity Biomedical Sciences Institute, Trinity College Dublin, Dublin, Ireland. [91]Department of Pediatrics, Graduate School of Biomedical and Health Sciences, Hiroshima University, Hiroshima, Japan. [92]Health Science Research and Development Center (HeRD), Institute of Science Tokyo (Science Tokyo), Tokyo, Japan. [93]Department of Molecular Biology and Genetics, Bilkent University, Ankara, Turkey. [94]Department of Medical Genetics, School of Medicine, Erciyes University, Kayseri, Turkey. [95]Institute of Biomedical Research of IdiPAZ, University Hospital "La Paz", Madrid, Spain. [96]Center for Biomedical Research on Respiratory Diseases (CIBERES), Instituto de Salud Carlos III, Madrid, Spain. [97]CIBERNED, Network Center for Biomedical Research in Neurodegenerative Diseases, National Institute of Health Carlos III, Madrid, Spain. [98]Unitat de Genètica Molecular, Institut de Biomedicina de València-CSIC, Valencia, Spain. [99]Center for Discovery and Innovation, Hackensack Meridian Health, Nutley, NJ, USA. [100]University of Cape Town Lung Institute, Cape Town, South Africa. [101]Groote Schuur Hospital, University of Cape Town, Cape Town, South Africa. [102]IIBB-CSIC, IDIBAPS, Barcelona, Spain. [103]Faculty of Pequeno Príncipe, Pesquisa Pelé Pequeno Príncipe Institute, Curitiba, Brazil. [104]Neurometabolic Diseases Laboratory, Institut d'Investigació Biomèdica de Bellvitge (IDIBELL), Hospital Duran i Reynals, Barcelona, Spain. [105]Center for Biomedical Research on Rare Diseases, (CIBERER U759) Ministry of Science Innovation and University, Madrid, Spain. [106]Catalan Institution of Research and Advanced Studies (ICREA), Barcelona, Spain. [107]Human Evolutionary Genetics Unit, CNRS U2000, Institut Pasteur, Paris, France. [108]Human Genomics and Evolution, Collège de France, Paris, France. [109]Al Jalila Children's Hospital, Dubai, United Arab Emirates. [110]University Hospital St. Marina, Varna, Bulgaria. [111]Department of Immunology, University Hospital of Gran Canaria Dr. Negrín, Canarian Health System, Las Palmas de Gran Canaria, Spain. [112]Department of Medical and Surgical Sciences, School of Medicine, Universidad de Las Palmas de Gran Canaria, Las Palmas de Gran Canaria, Spain. [113]Department of Clinical Sciences, University Fernando Pessoa Canarias, Las Palmas de Gran Canaria, Spain. [114]CIBER de Enfermedades Respiratorias (CIBERES), Instituto de Salud Carlos III, Madrid, Spain. [115]Department of Paediatric Infectious Diseases and Virology, Imperial College London, London, UK. [116]Centre for Paediatrics and Child Health, Faculty of Medicine, Imperial College London, London, UK. [117]Department of Immunology, Second Faculty of Medicine, Charles University and University Hospital in Motol, Prague, Czechia. [118]Adult Immunodeficiency Unit, Infectious Diseases, Inflammation Center, University of Helsinki and Helsinki University Hospital, Helsinki, Finland. [119]Rare Diseases Center and Pediatric

Research Center, Children's Hospital, University of Helsinki and Helsinki University Hospital, Helsinki, Finland. [120]Dr. Shahrooei Lab, Tehran, Iran. [121]Department of Immunology, Dmitry Rogachev National Medical Research Center of Pediatric Hematology, Oncology and Immunology, Moscow, Russia. [122]Central European Institute of Technology & Department of Biology, Faculty of Medicine, Masaryk University, Brno, Czechia. [123]Department of Pharmacology & Molecular Therapeutics, Uniformed Services University of the Health Sciences, Bethesda, MD, USA. [124]Pediatric Infectious Diseases and Immunodeficiencies Unit, Vall d'Hebron Barcelona Hospital Campus, Barcelona, Catalonia, Spain. [125]Université de Paris, Institut de Recherche Saint-Louis, INSERM U976, Hôpital Saint-Louis, Paris, France. [126]AP-HP, Hôpital Saint-Louis, Laboratoire d'Immunologie, Paris, France. [127]Department of Medical Microbiology, University Medical Center Utrecht, Utrecht University, Utrecht, The Netherlands. [128]Department of Internal Medicine II, Medical University of Innsbruck, Innsbruck, Austria. [129]Garvan Institute of Medical Research, Darlinghurst, NSW, Australia. [130]St Vincent's Clinical School, Faculty of Medicine, UNSW Sydney, Sydney, NSW, Australia. [131]Department of Translational Medicine, Institute of Health Sciences & Department of Medical Genetics, Faculty of Medicine, Bursa Uludag University, Bursa, Turkey. [132]Etablissement Francais Du Sang, La Plaine-Saint Denis, Paris, France. [133]Hospices Civils de Lyon, Lyon, France. [134]International Center of Research in Infectiology, Lyon University, INSERM U1111, CNRS UMR 5308, ENS, UCBL, Lyon, France. [135]BC Children's Hospital, The University of British Columbia, Vancouver, BC, Canada. [136]Centre for Precision Therapeutics, Genetics & Genomic Medicine Centre, NeuroGen Children's Healthcare and Lecturer, Holy Family Red Crescent Medical College Dhaka, Dhaka, Bangladesh. [137]College of Medicine, Mohammed Bin Rashid University of Medicine and Health Sciences, Dubai, United Arab Emirates. [138]Cellular Intelligence (Ci) Lab, GenomeArc Inc., Toronto, ON, Canada. [139]Department of Neurology, Amsterdam Neuroscience, Amsterdam University Medical Center, University of Amsterdam, Amsterdam, The Netherlands. [140]Hospital de Clínicas de Porto Alegre, Centro de Pesquisa Experimental, Laboratório de Medicina Genômica, Porto Alegre, Brazil. [141]Programa de Pós-Graduação em Genética e Biologia Molecular, Instituto de Biociências, Departamento de Genética, Laboratório de Imunogenética, Universidade Federal do Rio Grande do Sul, Porto Alegre, Brazil. [142]Department of Medicine, Division of Infectious Diseases, McGill University Health Centre, Montréal, QC, Canada. [143]Infectious Disease Susceptibility Program, Research Institute, McGill University Health Centre, Montréal, QC, Canada. [144]Department of Pediatric Pneumology, Immunology and Intensive Care, Charité Universitätsmedizin, Berlin University Hospital Center, Berlin, Germany. [145]Labor Berlin GmbH, Department of Immunology, Berlin, Germany. [146]Berlin Institutes of Health (BIH), Berlin-Brandenburg Center for Regenerative Therapies, Berlin, Germany. [147]Department of General Internal Medicine, Medical Intensive Care Unit, University Hospitals Leuven, Leuven, Belgium. [148]Human Genome and Stem Cell Research Center, Institute of Biosciences, University of São Paulo, São Paulo, São Paulo, Brazil. [149]Department of Infectious Diseases, Aalborg University Hospital, Aalborg, Denmark. [150]Department of Infectious Diseases, Hvidovrere hospital, Hvidovre, Denmark. [151]Department of Infectious Diseases, Rigshospitalet, Copenhagen, Denmark.